PNAS nexus

Supporting Information for

Dynamics of Nanocluster Aerosol in the Indoor Atmosphere During Gas Cooking

Satya S. Patra[a,b], Jinglin Jiang[a,b], Xiaosu Ding[a], Chunxu Huang[a,b], Emily K. Reidy[c], Vinay Kumar[d], Paige Price[d], Connor Keech[e], Gerhard Steiner[f], Philip Stevens[c,d], Nusrat Jung[a*], and Brandon E. Boor[a,b*]

[a]Lyles School of Civil Engineering, Purdue University, West Lafayette, Indiana 47907, United States.

[b]Ray W. Herrick Laboratories, Center for High Performance Buildings, Purdue University, West Lafayette, Indiana 47907, United States.

[c]Department of Chemistry, Indiana University, Bloomington, Indiana 47405, United States.

[d]O'Neill School of Public and Environmental Affairs, Indiana University, Bloomington, Indiana 47405, United States.

[e]DURAG Inc., Minnetonka, Minnesota 55343, United States.

[f]GRIMM Aerosol Technik Ainring GmbH & Co. KG, Ainring 83404, Germany.

***Corresponding Authors:** Nusrat Jung and Brandon E. Boor.

Email: nusratj@purdue.edu and bboor@purdue.edu

This PDF file includes:

Supporting Information Text

Study Site Description: Purdue zEDGE Test House

The measurement campaign was conducted in a single-zone, mechanically ventilated residential building – the Purdue zero Energy Design Guidance for Engineers (zEDGE) test house (Fig. S2) (1–3). The Purdue zEDGE test house is located on the Purdue University campus in West Lafayette, Indiana, U.S., and is constructed on a mobile trailer in accordance with Recreational Vehicle Industry Association (RVIA) guidelines and maintains a National Organization of Alternative Housing (NOAH) certification. The total conditioned interior volume of zEDGE is 60.35 m^3, divided into two areas – the main floor and the loft area (Fig. S2). zEDGE is equipped with a single-zone ductless heating and cooling system (FTX12NMVJU, Daikin North America LLC, Houston, TX, U.S.). The nominal outdoor air ventilation rate was 0.45 h^{-1} during the field campaign (Table S1). Four mixing fans were installed on the main floor and the loft area of zEDGE to promote the mixing of indoor air (Fig. S3). Mixing was evaluated using four co-located battery-powered diffusion chargers (Pegasor AQ Indoor, Pegasor Oy, Tampere, Finland), each having an operational range of 10 to 2,500 nm. During a propane gas cooking experiment, the comparison of total particle number concentrations recorded by the diffusion chargers at different locations is shown in Figure S3. The good agreement in the comparison suggests well-mixed indoor air conditions in the test house due to the use of the four mixing fans.

High-Resolution Online Nanoparticle Measurements

Indoor particle number concentrations and size distributions from 1.18 to 30,000 nm were measured using a suite of online aerosol instrumentation, including a novel particle size magnifier – scanning mobility particle sizer (PSMPS; GRIMM Aerosol Technik Ainring GmbH & Co. KG, Ainring, Germany), a SMPS with a long-differential mobility analyzer (DMA) (Model 3938NL88, TSI Inc., Shoreview, Minnesota, U.S.), and a wideband integrated bioaerosol sensor (WIBS; Model WIBS-NEO, Droplet Measurement Technologies LLC, Longmont, Colorado, U.S.). The layout of the aerosol instrumentation in the Purdue zEDGE test house is shown in Fig. S3.

The PSMPS is a new mobility particle size spectrometer for electrical mobility-classified measurements of atmospheric nanocluster aerosol (NCA). The PSMPS is configured with a soft X-ray neutralizer (Model 5524-X, GRIMM Aerosol Technik Ainring GmbH & Co. KG, Ainring, Germany), a Vienna-type modified short-DMA (S-DMA; GRIMM Aerosol Technik Ainring GmbH & Co. KG, Ainring, Germany), a diethylene glycol-based PSM (Model A10, Airmodus Ltd., Helsinki, Finland), and a butanol-based condensation particle counter (CPC; Model 5417, GRIMM Aerosol Technik Ainring GmbH & Co. KG, Ainring, Germany) (Fig. S2). The PSMPS samples particles at a flow rate of 2.5 L min^{-1}. Each sample stream passes through the soft X-ray neutralizer that conditions the particles to a known charging state (4), after which the particles reach the S-DMA. The modified S-DMA operates at a sample flow rate of 2.5 L min^{-1} and a sheath flow rate of 10 L min^{-1} to classify the particles based on their electrical mobility in the size range of 1.18 to 55.7 nm (electrical mobility diameter). The sheath air is dried using a sheath air dryer (Model 5540, GRIMM Aerosol Technik Ainring GmbH & Co. KG, Ainring, Germany) that utilizes silica gel as the drying agent. Following electrical mobility classification, particle growth and detection is performed via the PSM and CPC. First, the PSM uses diethylene glycol as the condensing fluid to activate particles down to 1.18 nm. In the CPC, particles are further grown to sizes that scatter light efficiently to facilitate optical detection. An optical cell in the CPC counts the grown particles by detecting the amount of light scattered. The PSMPS is controlled by a custom data acquisition software (LabVIEW, National Instruments Corp., Austin, Texas, U.S.).

The SMPS includes a Kr-85 bi-polar charger (370 MBq, Model 3077A, TSI Inc., Shoreview, Minnesota, U.S.), a long-DMA (Model 3081, TSI Inc., Shoreview, Minnesota, U.S.), and a water-based CPC (Model 3788, TSI Inc., Shoreview, Minnesota, U.S.). The SMPS was used to classify and detect particles in the size range of 13.1 to 572.5 nm (electrical mobility diameter). Lastly, particles from 500 to 30,000 nm (optical equivalent diameter) were measured using the WIBS. The WIBS uses a 635 nm continuous laser diode to detect and size particles. A detailed description of the WIBS can be found

elsewhere (5). Additional air quality instrumentation used in this study includes a NO_x (NO and NO_2) analyzer (Model 42C, Thermo Electron Corp., Waltham, MA, U.S.), a CO_2 analyzer (Model LI-830, LI-COR Biosciences, Lincoln, NE, U.S.), and a handheld humidity and temperature meter (Model HM70, Vaisala Oyj, Helsinki, Finland).

Field Measurement Campaign Experimental Protocol

During the field measurement campaign, a total of n=12 propane gas cooking events were evaluated in the Purdue zEDGE test house using a two-burner propane (C_3H_8) gas stove, including boiling water (n=6), cooking buttermilk pancakes (n=3), and cooking grilled cheese (n=3). The gas stove features two fully adjustable burners with a maximum output of 10,000 BTU each. Constructed entirely of metal, it measures 56 cm in length, 33 cm in width, and 10 cm in height. The cooking experiments were conducted using propane gas as the fuel. We used an electronic handheld lighter for ignition.

Propane gas cooking experiments started at time zero, with two experimenters entering the Purdue zEDGE test house. During the initial 10 minutes, no activities were performed in the test house in order to establish a baseline concentration of indoor air pollutants with people present. At the 10-minute mark, the propane gas stove was ignited using an electronic handheld lighter. The cooking process was then carried out for the following 20 minutes. At the 30-minute mark, the propane gas stove was shut down, and the experimenters exited the test house carrying the prepared food. Finally, we observed a decay in the emitted air pollutants in the unoccupied test house over a period from 30 to 150 minutes. For the boiling water experiments, water was boiled for 20 min on the gas stove in a stainless steel pot. For the buttermilk pancake experiments, batter was prepared using milk, buttermilk, egg, vegetable oil, and pancake mix. This mixture was added to a hot, butter-greased cast iron skillet and cooked for 2.5 min on each side. Three buttermilk pancakes were cooked during the active combustion period. For the grilled cheese events, sandwiches were grilled over a hot, butter-greased cast iron skillet. For simplicity, the propane gas combustion experiments were divided into two categories: boiling water (n=6, including all boiling water events) and cooking (n=6, including the buttermilk pancake and grilled cheese cooking events). The indoor air conditions in the Purdue zEDGE test house for each event are summarized in Table S1.

Data Analysis

The PSMPS data acquisition software provided particle number size distributions ($dN/d\log D_p$; cm^{-3}) at 2 min S-DMA scan intervals for particles from 1.18 to 55.7 nm across 108 size bins. The data acquisition software corrected this data for the charging efficiency of the soft X-ray neutralizer, DMA penetration, and the combined PSM and CPC counting efficiency. An additional correction for diffusional losses for the soft X-ray neutralizer was performed using equations for particle penetration through a circular tube developed by Gormley and Kennedy (1948) (6), assuming an equivalent length of 2.4 m for the soft X-ray neutralizer (7).

The PSMPS classifies particles based on their electrical mobility, which requires pre-classification particle charging. This is achieved using the soft X-ray neutralizer. During charging, the soft X-ray source's electric charge can collide with carrier gas molecules, generating charged gas ions, or charger ions (8, 9), in the NCA size fraction. These charger ions overlap in size with sample particles and show up in the final particle number size distribution output of the PSMPS. Additional physical transformations, such as charge transfer, evaporation, clustering, and fragmentation, may occur inside the instrument due to charger ion interactions with sample particles, further impacting the final particle number size distribution (8, 10–12). Consequently, distinguishing between charger ions and sample particles in the final particle number size distribution is challenging. It is essential to eliminate such interferences to accurately identify the NCA concentration elevation attributable solely to propane gas combustion.

A single-value subtraction based on background concentrations from all events during the background period may not effectively remove charger ion interferences, as the involved physical transformations

are not fully understood. Instead, a data-driven, event-specific correction is employed in this study. In the data analysis, the sub-3 nm bin concentrations during gas stove operation are only considered if they surpass the background number concentrations (13). To confidently evaluate particle elevation in the indoor atmosphere caused by gas combustion, a threshold representing the 85th percentile of both the background number concentration and the concentration at the decay period's end is determined for each sub-3 nm bin for every event. The calculated threshold number concentration is then subtracted from the corresponding bin's number concentration. The resulting concentration is used in the final NCA particle number size distribution, potentially free from background NCA and charger ion peaks. Fig. S4 illustrates an example of the threshold estimation for a sub-3 nm bin during a gas combustion event. After applying the threshold correction, the mean noise-to-signal ratio, defined by the ratio of the mean NCA number concentration during the decay to that during the active combustion period, was 0.16 across all the propane gas cooking experiments. This ratio can be considered as the noise-to-signal ratio for propane gas combustion experiments due to the extremely short lifetime of NCA and the absence of a NCA source after the gas stove is switched off.

This data-driven method for charger ion correction has the advantage of not requiring specific knowledge of charger ion physical transformation processes; instead, it relies on event-specific data. However, it should be noted that background charger ion concentrations might differ from those during gas stove emission periods. Prior studies on flame-generated aerosol have reported that charger ion concentrations decrease when the flame is turned on, as elevated particle concentrations consume excess charge (10). Consequently, this correction might underestimate NCA concentrations. The literature lacks established methods for discriminating charger ions from sample particles. While the proposed data-driven method has certain limitations, it can serve as one approach for addressing charger ions in the final NCA number size distributions. Additional research is needed to develop a method for discriminating charger ions in measurements based on electrical mobility classification of NCA. The NCA data analysis approach presented in this study is therefore sensitive to this correction method and may vary if alternative methods are used. The final number concentration output of the PSMPS for the gas combustion events is obtained after the corrections by the data acquisition software, the diffusional loss correction for the soft X-ray neutralizer, and the threshold correction for the sub-3 nm bins.

Particle number size distributions from the SMPS in the size range of 13.1 to 200 nm were used without any modification from the data acquisition software provided by the manufacturer (Aerosol Instrument Manager, TSI Inc., Shoreview, Minnesota, U.S.). Due to the operational limitations of the SMPS (14–16), particle number size distributions from 200 to 572 nm were estimated using spline interpolation. The SMPS operated with a 2 min long-DMA scan time. Finally, particle number size distributions from the WIBS in the size range of 500 to 30,000 nm were obtained using a custom program written in the Python environment. A detailed description on WIBS data processing can be found elsewhere (5). The WIBS provided data at >1 Hz time-resolution; this was aggregated and averaged every 2 min to match the time-resolution of the PSMPS and SMPS. The particle number size distributions from the PSMPS and SMPS in the overlapping size range (13.1 to 55.7 nm) showed reasonable agreement (Fig. S16) and were merged using a moving average smoothing approach. Finally, a continuous, wide size-range particle number size distribution was obtained, spanning from 1.18 to 30,000 nm. This included PSMPS data alone from 1.18 to 13.1 nm, moving average merged data from the PSMPS and SMPS from 13.1 to 55.7 nm, SMPS data from 55.7 to 500 nm, and WIBS data from 500 to 30,000 nm. Unusual outliers were removed from the time-resolved particle number size distributions. Particles from 1.18 to 500 nm are classified according to their electrical mobility diameter, and those from 500 to 30,000 nm according to their optical equivalent diameter.

The merged particle number size distributions ($dN/d\log D_p$; cm^{-3}) were converted to particle surface area size distributions ($dS/d\log D_p$; $\mu m^2\ cm^{-3}$) assuming spherical particles (dynamic shape factor: χ = 1) and particle mass size distributions ($dM/d\log D_p$; $\mu g\ m^{-3}$) assuming the particle effective densities listed in Table S2. The particle mass size distributions were then size-integrated from 1.18 to 2,500 nm to obtain $PM_{2.5}$ mass concentrations ($\mu g\ m^{-3}$). The aerosol Fuchs surface area (A_{Fuchs}; $\mu m^2\ cm^{-3}$), a coagulation scavenging parameter based on kinetic theory (17), was also calculated using the merged particle number size distributions using Eq. 1 as:

$$A_{\text{Fuchs}} = \frac{4\pi}{3}\int_{d_p=1.18\,nm}^{d_p=2500\,nm} d_p^2 \cdot \left(\frac{Kn+Kn^2}{1+1.71Kn+1.33Kn^2}\right) \cdot \frac{dN}{dlogD_p} \cdot dlogD_p \quad (1)$$

where *Kn* is the particle Knudsen number. Differentiating Eq. 1 with respect to dlogD_p, the aerosol Fuchs surface area size distribution (dA_{Fuchs}/dlogD_p; μm^2 cm^{-3}) is obtained as:

$$\frac{dA_{Fuchs}}{dlogD_p} = \frac{4\pi}{3} \cdot d_p^2 \cdot \left(\frac{Kn+Kn^2}{1+1.71Kn+1.33Kn^2}\right) \cdot \frac{dN}{dlogD_p} \quad (2)$$

Eq. 2 can also be written as:

$$\frac{dA_{Fuchs}}{dlogD_p} = F_M \frac{dS}{dlogD_p} \quad (3)$$

where $F_M = \frac{4}{3} \cdot \left(\frac{Kn+Kn^2}{1+1.71Kn+1.33Kn^2}\right)$. Hence, the aerosol Fuchs surface area size distribution is the product of a size-dependent multiplier (F_M) and the particle surface area size distribution (dS/dlogD_p). Fig. S5 illustrates the relationship between F_M and particle diameter. It is evident that F_M decreases as particle size increases, with a maximum value of 1. Thus, the value of the aerosol Fuchs surface area size distribution is always less than or equal to the value of particle surface area size distribution, and the aerosol Fuchs surface area is less than the size-integrated aerosol surface area concentration.

The NO_x analyzer recorded indoor NO and NO_2 mixing ratios at 1 Hz time-resolution, which was then time-averaged every 2 min. Similarly, the CO_2 analyzer logged indoor CO_2 mixing ratios at 1 Hz time-resolution. The decay in the indoor CO_2 mixing ratio after the gas stove was turned off during the unoccupied decay period was used to determine the outdoor air ventilation rate for each event (1, 2).

Size-Resolved Indoor Atmospheric NCA Dynamics Model

The emission rate is a generalizable metric that quantifies the number of species emitted per unit time. Herein, the apparent emission rate of NCA to the indoor atmosphere during propane gas cooking is estimated ($E_{NCA,app}$; min^{-1}). In this analysis, the combined gas stove flame and boiling water or cooking process is treated as a single emission source. The NCA emitted from the gas stove flame interacts with the particles emitted from the boiling water/cooking process, with $E_{NCA,app}$ representing the net flux of NCA persisting in the indoor bulk air after this interaction. This can be calculated using the aerosol general dynamic equation (GDE) in discrete space (18, 19), and the NCA number concentrations and size distributions in the bulk indoor air as measured with the PSMPS.

In the aerosol GDE, the temporal rate of change in the total number of particles ($N_{d_{p,i}}$) that persisted in the indoor bulk air in size bin i, as measured by the PSMPS, is equal to the source terms minus the loss terms, expressed as:

$$\frac{dN_{d_{p,i}}}{dt} = source\ terms - loss\ terms \quad (4)$$

All particles in a size bin i are characterized by the midpoint diameter, d_p, which represents the average diameter between the boundaries of the bin and is used in the GDE computations. Table S8 provides the bin boundaries and the midpoint diameters of the NCA size bins of the PSMPS. The loss terms in Eq. 4 include: outdoor air ventilation, deposition onto indoor surfaces via Brownian and turbulent diffusion, coagulation scavenging by larger particles, and condensational flux out of the size bin i (20). The source terms in Eq. 4 include: the apparent emission rate ($E_{d_p,app}$; cm^{-3} min^{-1}) of particles at size d_p formed via the gas combustion process, the formation of particles at size d_p due to coagulation among smaller particles (21) ($CoagSrc_{d_p}$; cm^{-3} min^{-1}), and the condensational flux into size

bin i, with midpoint diameter d_p. Combining the source and loss terms, the aerosol GDE for particles at size d_p during the gas stove combustion events can be written as:

$$\frac{dN_{d_{p,i}}}{dt} = E_{d_{p,app}}\,[cm^{-3}min^{-1}] + coagulation\ source + condensation\ source - ventilation\ loss - deposition\ loss - coagulation\ loss - condensation\ loss \quad (5)$$

By rearranging the terms of Eq. 5, the apparent emission rate ($E_{d_{p,app}}$) of particles at size d_p can be written as:

$$E_{d_{p,app}}\,[cm^{-3}min^{-1}] = \frac{dN_{d_{p,i}}}{dt} + ventilation\ loss + deposition\ loss + coagulation\ loss + condensation\ loss - coagulation\ source - condensation\ source \quad (6)$$

The time derivative of the number concentration of size bin i ($dN_{d_{p,i}}/dt$, cm^{-3} min^{-1}) is computed by fitting the number concentration data in the size bin with a Gaussian kernel, and then dividing the difference between the fitted number concentrations of two consecutive time intervals by the duration of the interval. The loss of particles due to ventilation is obtained as:

$$ventilation\ loss = k_{vent} \cdot N_{d_{p,i}} \quad (7)$$

where k_{vent} [min^{-1}] is the outdoor air ventilation rate (nominally 0.45 h^{-1}). The loss of particles due to deposition onto indoor surfaces via Brownian and turbulent diffusion is expressed as:

$$deposition\ loss = k_{dep,d_p} \cdot N_{d_{p,i}} \quad (8)$$

where k_{dep,d_p} [min^{-1}] is the size-dependent first-order deposition loss rate coefficient of particles at size d_p. As there did not exist suitable NCA concentration decay curves following the 20 min active combustion period (Fig. 1), the size-dependent first-order deposition loss rate coefficient could not be estimated via traditional curve-fitting techniques. Thus, k_{dep,d_p} was estimated using the Lai and Nazaroff (2000) (22) indoor particle deposition model. The input parameters for the model include: the friction velocity (v_f; cm s^{-1}), volume of the room (V, cm^3), area of vertical-facing surfaces (a_v; m^2), area of upward-facing horizontal surfaces (a_u; m^2), and area of downward-facing horizontal surfaces (a_d; m^2). For the zEDGE test house and considering all instrumentation, equipment, and surfaces, these parameters were estimated as: volume = 60.35 m^3, a_v = 79.11 m^2, a_u = 21.47 m^2, and a_d = 21.10 m^2. The friction velocity for the established mixing conditions was estimated by measuring the bulk indoor air velocity using a hot wire anemometer. v_f was determined to be 1.22 cm s^{-1}. Using these values as inputs into the Lai and Nazaroff model (2000), the size-dependent first-order deposition loss rate coefficient, k_{dep,d_p}, was estimated.

The loss of particles via coagulation onto existing particles is expressed as:

$$coagulatuion\ loss = CoagSnk_{d_p} \cdot N_{d_{p,i}} \quad (9)$$

where $CoagSnk_{d_p}$ (min^{-1}) is the coagulation sink of particles at size d_p. $CoagSnk_{d_p}$ is expressed as:

$$CoagSnk_{d_p} = \sum_{d'_p=1.18\ nm}^{d'_p=2500\ nm} k_{coag}(d_p, d'_p) \cdot N_{d'_{p,i}} \quad (10)$$

where $k_{coag}(d_p, d'_p)$ is the coagulation coefficient between particles at sizes d_p and d'_p ($cm^3\ min^{-1}$). $N_{d'_{p,i}}$ is the number concentration in size bin i with midpoint diameter d'_p. $k_{coag}(d_p, d'_p)$ is calculated using the Brownian and van der Waals viscous forces coagulation model (23). This model was experimentally determined to best represent indoor gas stove combustion.

For the boiling water experiments, where no condensational growth is expected because of the absence of a low-volatility vapor source and the non-hygroscopic nature of freshly nucleated soot particles (24) in the observed RH range (Figure S17), the Hamaker constant was estimated by a novel retrofitting approach. In this approach, first, the apparent growth rate (GR_{App,d_p}) from the particle number size distributions during the boiling water experiments is obtained using the mode-fitting method (19, 25). GR_{App,d_p} was then corrected for intermodal coagulation as suggested by Leppä et al. (26) to obtain the total growth rate (GR_{Tot,d_p}) (25). As there is no condensation, this GR_{Tot,d_p} should be equal to the coagulation growth rate. The theoretical intramodal coagulation growth rate (GR_{Coag,d_p}) can be expressed as (27):

$$GR_{Coag,d_p} = \sum_{d'_p = 1.18\ nm}^{d'_p = d_p} k_{coag}(d'_p, d_p) \cdot N_{d'_{p,i}} \cdot \left[\sqrt[3]{{d'_p}^3 + {d_p}^3} - d_p\right] \quad (11)$$

In Eq. 11, we adjusted the Hamaker constant values to obtain the best fit between GR_{Coag,d_p} and GR_{Tot,d_p}. It should be noted that the intermodal coagulation correction for GR_{Tot,d_p} also requires a Hamaker constant value. Hence, the Hamaker constant value was obtained iteratively. The best fit Hamaker constant (2.6×10^{-19} J) for a representative boiling water experiment comparing GR_{Tot,d_p} and GR_{Coag,d_p} is shown in Figure S18. The estimated Hamaker constant value is within the range reported by Falco et al. (28) for flame-formed carbon nanoparticles. For the cooking experiments, the Hamaker constant used is summarized in Table S3. Fig. S6 presents the $k_{coag}(d_p, d'_p)$ for the boiling water and cooking events considering the Hamaker constants listed in Table S3.

The formation of particles due to coagulation among smaller particles ($CoagSrc_{d_p}$) is expressed as:

$$CoagSrc_{d_p} = \sum_{{d_p}^3 = {d'_p}^3 + {d''_p}^3}^{d'_p,\, d''_p < d_p} 0.5 \cdot k_{coag}(d'_p, d''_p) \cdot N_{d'_{p,i}} \cdot N_{d''_{p,j}} \quad (12)$$

where d'_p and d''_p are particles with sizes smaller than d_p which coagulate to form particles at size d_p, and $N_{d'_{p,i}}$ and $N_{d''_{p,j}}$ are the corresponding number concentrations in size bins i and j with midpoint diameters d'_p and d''_p, respectively.

The net difference between $CoagSnk_{d_p}$ and $CoagSrc_{d_p}$, represented as $CoagSnk_{Net,d_p}$ (min^{-1}), effectively captures the coagulation scavenging effect of particles at size d_p (21). $CoagSnk_{Net,d_p}$ is calculated as:

$$CoagSnk_{Net,d_p} = CoagSnk_{d_p} - \frac{CoagSrc_{d_p}}{N_{d_{p,i}}} \quad (13)$$

For this analysis, $CoagSnk_{Net}$ represents the median value of $CoagS_{Net,d_p}$ for 1.18 nm $< d_p <$ 3 nm.

The condensation loss of particles at size d_p is the condensational particle flux from size bin i, with midpoint diameter d_p, to the next size bin due to the condensation of low-volatility cooking vapors (20). This is parametrized as:

$$Cond_{d_{p,i}} = \frac{GR_{d_p}}{\Delta d_{p,i}} \cdot N_{d_{p,i}} \quad (14)$$

Similarly, the condensation source of particles in a size bin i, with midpoint diameter d_p, is the condensational particle flux from the previous size bin ($Cond_{(d_{p,i-1})}$). In Eq. 14, $\Delta d_{p,i}$ is the width of the size bin i and GR_{d_p} is the net condensational growth rate of particles at size d_p (GR_{Cond,d_p}; nm min^{-1}), calculated using the mode-fitting method (19, 25) and is corrected for the growth rate due to intramodal coagulation (GR_{Coag,d_p}), as shown in Eq. 12, and intermodal coagulation (GR_{Scav,d_p}), as suggested by Leppä et al. (26). A detailed explanation of various growth rates can be found elsewhere (25). Condensational particle growth is considered only in butter-based cooking experiments (buttermilk pancakes and grilled cheese) due to the emission of low-volatility cooking vapors (29). The mode-fitted diameters for a representative butter-based cooking measurement are shown in Figure S19. Additionally, all the growth rate corrections for the same experiment are shown in the figure. The sub-3 nm size range lacked a well-defined mode; therefore, for particles smaller than 3 nm, the condensational growth rate was approximated using a single value extrapolation. This was based on the condensational growth rate value obtained for the particles at size d_p closest to 3 nm.

Using Eqs. 7, 8, 9, 10, 12, and 14, Eq. 6 can be simplified as:

$$E_{d_{p,app}}\,[cm^{-3}min^{-1}] = \frac{dN_{d_{p,i}}}{dt} + k_{vent} \cdot N_{d_{p,i}} + k_{dep,d_p} \cdot N_{d_{p,i}} + CoagSnk_{d_p} \cdot N_{d_{p,i}} - CoagSrc_{d_p} + Cond_{d_{p,i}} - Cond_{(d_{p,i-1})} \quad (15)$$

Eq. 15 formulates the apparent emission rate for particles at size d_p. Extending this to the NCA size fraction (1.18 nm ≤ d_p ≤ 3 nm), the indoor atmospheric apparent NCA emission rate ($E_{NCA,app}$; cm^{-3} min^{-1}) can be expressed as:

$$E_{NCA,app}[cm^{-3}min^{-1}] = \sum_{d_p=1.18\ nm}^{d_p=3\ nm} \left(\frac{dN_{d_{p,i}}}{dt} + k_{vent} \cdot N_{d_{p,i}} + k_{dep,d_p} \cdot N_{d_{p,i}} + CoagSnk_{d_p} \cdot N_{d_{p,i}} - CoagSrc_{d_p} + Cond_{d_{p,i}} - Cond_{(d_{p,i-1})} \right) \quad (16)$$

Since the smallest bin in which the PSMPS can detect particles is characterized by $d_p = 1.18$ nm, the lower limit of the coagulation source term that can be factored in is derived from the self-coagulation of particles in the smallest detectable size bin, resulting in particles at size $d_p = 1.46$ nm. Thus, the coagulation source is only computed for particle at sizes larger than 1.46 nm, and thus, the computation of apparent emission rates for sizes smaller than 1.46 nm does not feature the coagulation source term. Eq. 16 is further generalized to estimate the apparent emission rate of NCA per unit time by multiplying both sides of Eq. 16 by the indoor volume of the zEDGE test house (V, cm^3). Therefore, the final formulation of $E_{NCA,app}$ (min^{-1}) is expressed as:

$$E_{NCA,app}[min^{-1}] = V \cdot \sum_{d_p=1.18\ nm}^{d_p=3\ nm} \left(\frac{dN_{d_{p,i}}}{dt} + k_{vent} \cdot N_{d_{p,i}} + k_{dep,d_p} \cdot N_{d_{p,i}} + CoagSnk_{d_p} \cdot N_{d_{p,i}} - CoagSrc_{d_p} + Cond_{d_{p,i}} - Cond_{(d_{p,i-1})} \right) \quad (17)$$

Using data from the published literature, each term in Eq. 17 was validated for computation accuracy.

The relative contribution of each NCA source and loss term (*b*) to the size-resolved apparent emission rate can be expressed as:

$$Relative\ Contribution_{b,d_p} = \frac{|b|}{\left|\frac{dN_{d_{p,i}}}{dt}\right| + \left|k_{vent} \cdot N_{d_{p,i}}\right| + \left|k_{dep,d_p} \cdot N_{d_{p,i}}\right| + \left|CoagSnk_{d_p} \cdot N_{d_{p,i}}\right| + \left|CoagSrc_{d_p}\right| + \left|Cond_{d_{p,i}}\right| + \left|Cond_{(d_{p,i-1})}\right|} \quad (18)$$

Additionally, Fig. 3 suggests $E_{NCA,app}$ is sensitive to the coagulation loss term. Therefore, the sensitivity of $E_{NCA,app}$ relative to different values of the Hamaker constant was also assessed. In the sensitivity analysis, the Hamaker constant used in the coagulation model was varied as 20 k_BT and 200 k_BT (30) (where k_B is the Boltzmann constant) for the cooking experiments, and the corresponding errors in the $E_{NCA,app}$ and $CoagSnk_{Net}$ calculation relative to the values obtained using the assumed Hamaker constant (Table S3) was determined. The error values for two representative experiments (*n*=2 for cooking) are summarized in Tables S4 and S5.

Carbon Mass-Based Emission Factor Calculation

The particle number size distributions ($dN/d\log D_p$; cm^{-3}) and the size-integrated NCA number concentrations (N_{NCA}; cm^{-3}) were converted into emission factors using the following equation (31):

$$E_X = \frac{\Delta X}{\Delta CO_2} \cdot \frac{MW_{CO_2}}{AW_C} \cdot C_f \cdot 10^{15} \quad (19)$$

where ΔX is the background corrected particle number size distributions or size-integrated NCA number concentrations; ΔCO_2 is the background corrected CO_2 concentration in the test house in μg m^{-3}; MW_{CO_2} and AW_C are the molecular weight of CO_2 and atomic weight of carbon, respectively; and C_f is the mass fraction of carbon in the propane fuel (assumed as 0.85 g kg-$fuel^{-1}$ (31)).

For CO_2 background correction, a single-zone material balance model was developed to simulate the CO_2 concentrations in the test house, accounting for outdoor air ventilation and emissions from people via exhaled breath. The material balance model for CO_2 is as follows:

$$\frac{dCO_{2,in}}{dt}[mg\ m^{-3}h^{-1}] = n[p] \cdot E_{p,CO_2}[mg\ m^{-3}\ h^{-1}p^{-1}] + \left(CO_{2,out} - CO_{2,in}\right)[mg\ m^{-3}] \cdot k_{vent}[h^{-1}] \quad (20)$$

where $CO_{2,in}$ is the indoor CO_2 concentration [mg m^{-3}]; $CO_{2,out}$ is the outdoor CO_2 concentration [mg m^{-3}], which is considered to be constant and equal to the steady-state concentration after the CO_2 concentration decays to background following a combustion event; *n* is the number of people in the test house; and $E_{p,CO_2}$is the per person CO_2 emission rate [mg m^{-3} h^{-1} p^{-1}]. The analytical solution to the ordinary differential equation (Eq. 20) is:

$$CO_{2,in} = \left(CO_{2,t=0} - \frac{n \cdot E_{p,CO_2}}{k_{vent}} - CO_{2,out}\right) \cdot e^{-k_{vent} \cdot t} + \frac{n \cdot E_{p,CO_2}}{k_{vent}} + CO_{2,out} \quad (21)$$

As outlined in the experimental protocol section, there was a 10-minute period of no activity prior to the start of propane gas stove combustion (considered as the background period). Per-person CO_2 emission rates during light activity were reported to vary between 1.13–1.42 g m^{-3} h^{-1} p^{-1} (32). Eq. 21 was used with CO_2 emission rates within this range to best fit the observed CO_2 concentrations during the occupied background period. Thereafter, the model was run for the following 20 minutes to estimate the CO_2 flux from outdoor sources and occupant CO_2 emissions. This calculated CO_2 concentration was then subtracted from the CO_2 concentration observed during the 20-minute propane gas cooking experiment to determine the background-corrected CO_2 concentration. The background-

corrected CO_2 for all 12 experiments is shown in Fig S20. This background-corrected CO_2 concentration is used in Eq. 19 to estimate the NCA emission factors.

Calculation of Age-Specific Respiratory Tract Deposited Dose Rates

Respiratory tract deposited dose rates ($R_{D,NCA}$; min^{-1}) and cumulative respiratory tract deposited doses (D_{NCA}) of NCA were estimated to evaluate the rate of deposition and total deposition of NCA during propane gas combustion in different respiratory tract regions (head airways, tracheobronchial, pulmonary) of children and adults. Based on methods described in previous studies (2, 33), the size-resolved respiratory tract deposited dose rate ($dR_D/d\log D_p$; min^{-1}) can be expressed as:

$$\frac{dR_D}{dlogD_p} = Q \cdot DF_{d_p} \cdot \frac{dN}{dlogD_p} \quad (22)$$

where Q is the inhalation rate (m^3 min^{-1}) and DF_{d_p} is the size-resolved deposition fraction of particles in each respiratory tract region (head airways, tracheobronchial, pulmonary). Q is expressed as:

$$Q = f \cdot VT \quad (23)$$

where f is breathing frequency (breaths min^{-1}) and VT is tidal volume (cm^3). Table S9 summarizes breathing parameters during light intensity activities for children and adults. DF_{d_p} is obtained using the considered inhalation parameters in the Multiple-Path Particle Dosimetry (MPPD) model (v3.04, Applied Research Associates Inc., Albuquerque, New Mexico, U.S.) (shown in Fig. S7).

Size-integration of Eq. 22 between 1.18 and 3 nm yields the NCA respiratory tract deposited dose rate ($R_{D,NCA}$; min^{-1}):

$$R_{D,NCA} = \int_{d_p=1.18\ nm}^{d_p=3\ nm} Q \cdot DF_{d_p} \cdot \frac{dN}{dlogD_p} dlogD_p \quad (24)$$

For comparison purposes, $R_{D,NCA}$ and $dR_D/d\log D_p$ are normalized by body weights for children and adults (weight-normalized $R_{D,NCA}$ (min^{-1} kg^{-1}) and weight-normalized $dR_D/d\log D_p$ (min^{-1} kg^{-1})). The body weights used for normalization are provided in Table S9. Finally, the cumulative NCA respiratory tract deposited dose over a period t_1 to t_2 for each respiratory tract region is given by:

$$D_{NCA} = \int_{t1}^{t2} R_{D,NCA} \cdot dt \quad (25)$$

D_{NCA} was also normalized by the body weights of children and adults.

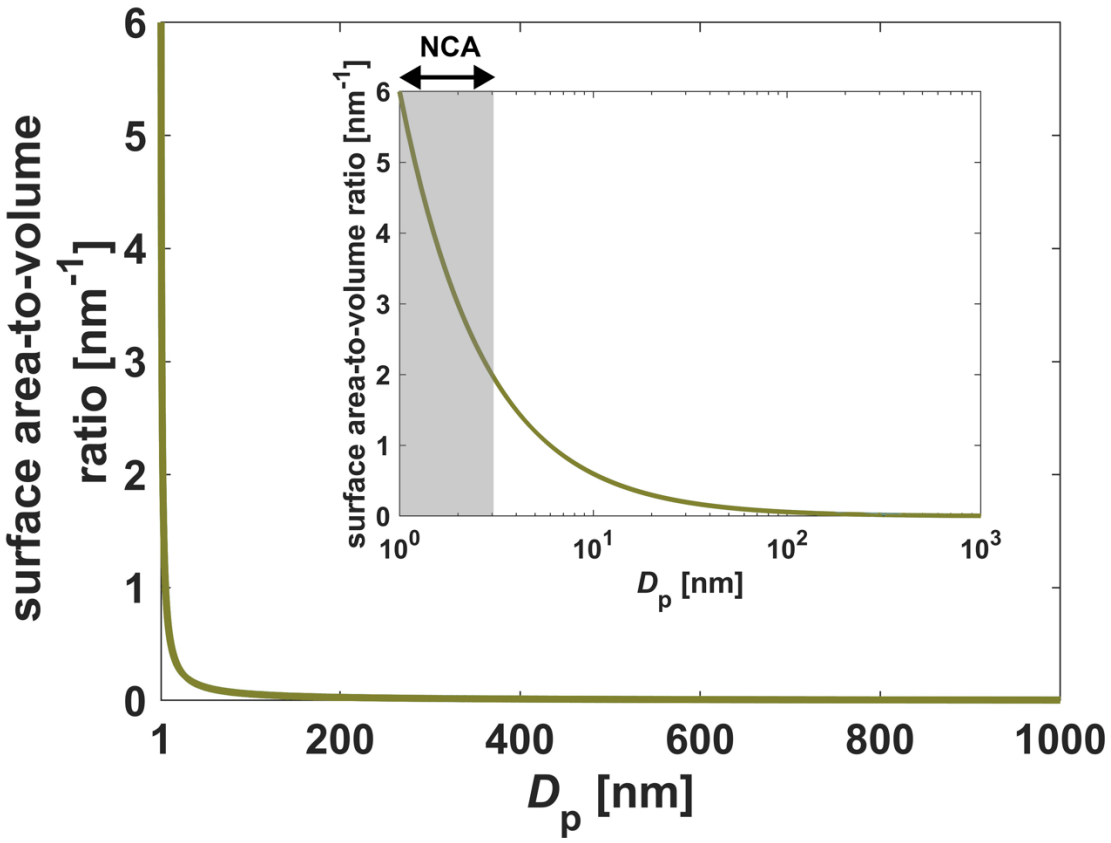

Figure S1. Surface area-to-volume ratio for sub-1,000 nm particles. The subplot presents the same results with a logarithmic x-axis. The shaded gray region highlights the NCA size fraction (1–3 nm). The surface area-to-volume ratio increases asymptomatically in the NCA size fraction.

Figure S2. (top-left) Purdue zEDGE test house, (top-right) PSMPS in the Purdue zEDGE test house, and (bottom) interior of Purdue zEDGE test house showing the main floor and loft area.

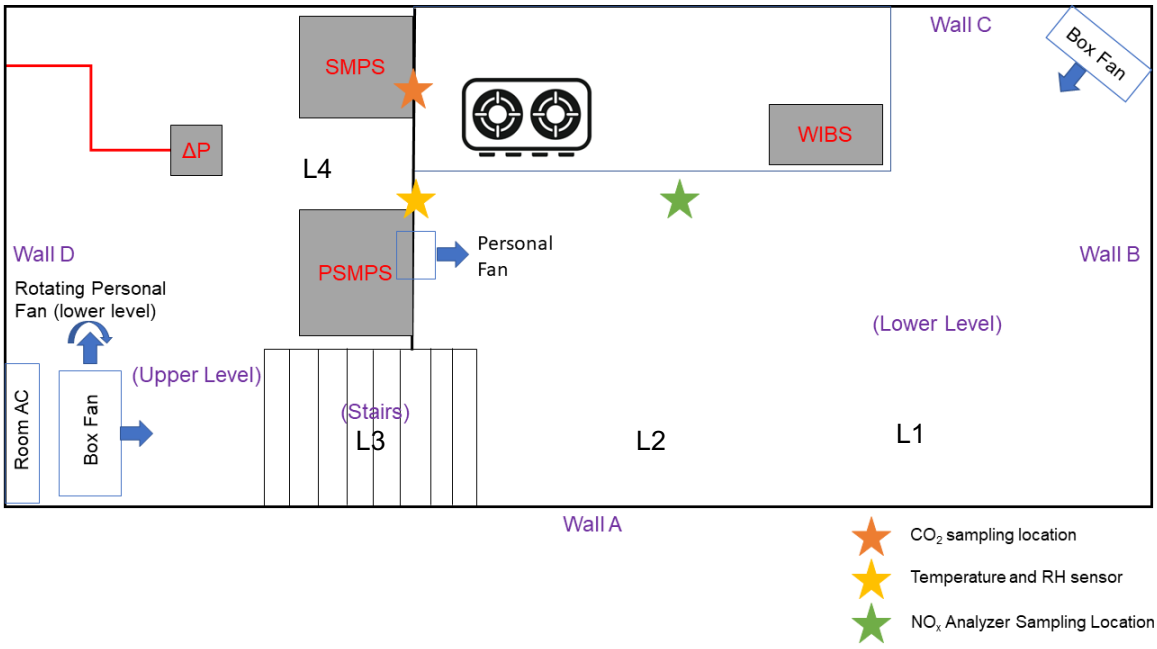

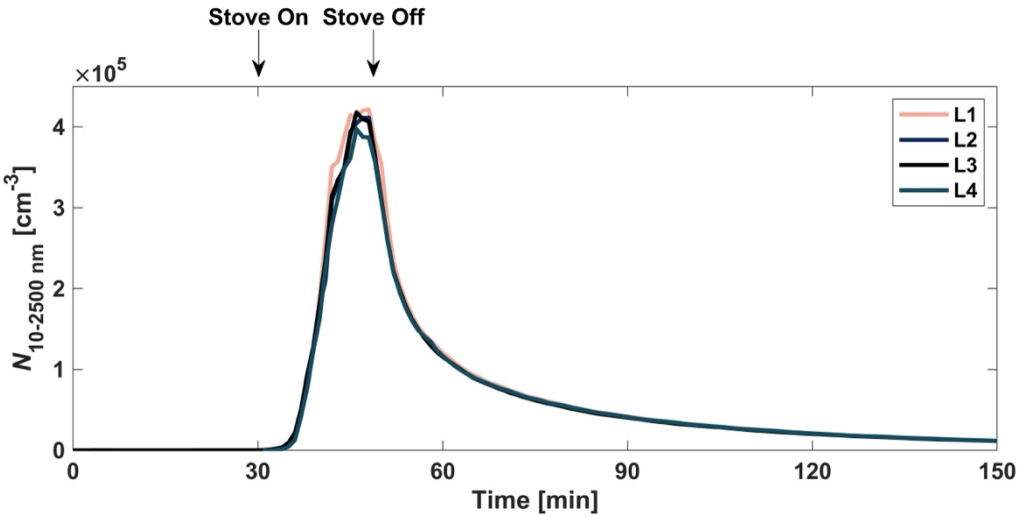

Figure S3. (top) Experimental layout of the Purdue zEDGE test house and aerosol instrumentation for the field measurement campaign. L1, L2, L3 and L4 represent the locations where four battery-powered diffusion chargers were placed to evaluate indoor air mixing of the Purdue zEDGE test house during propane gas cooking. (bottom) Comparison of the total particle number concentrations reported by the four diffusion chargers during a propane gas cooking event.

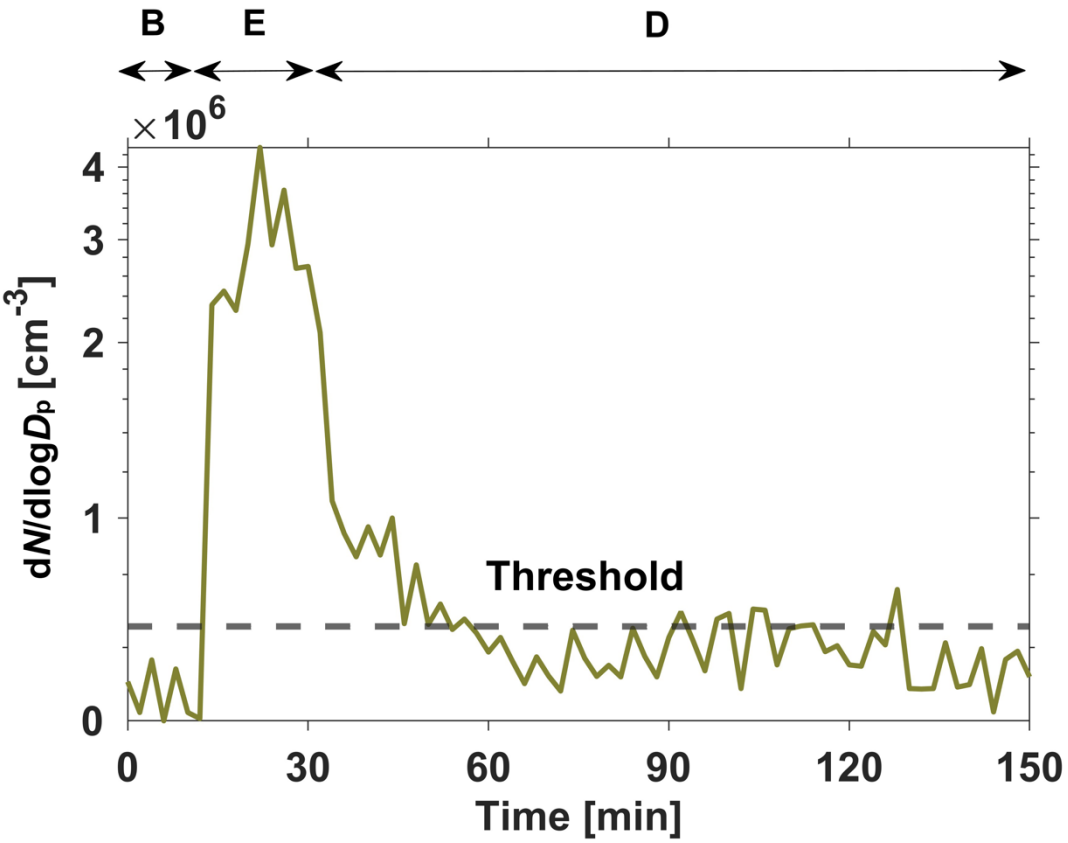

Figure S4. Representative example of the threshold estimation for a sub-3 nm bin to correct the particle number size distributions from background and charger ion interferences (B: 10-minute background period; E: emission event period (gas combustion active; gas stove was ignited at the beginning of this period and turned off at the end of this period); D: decay period).

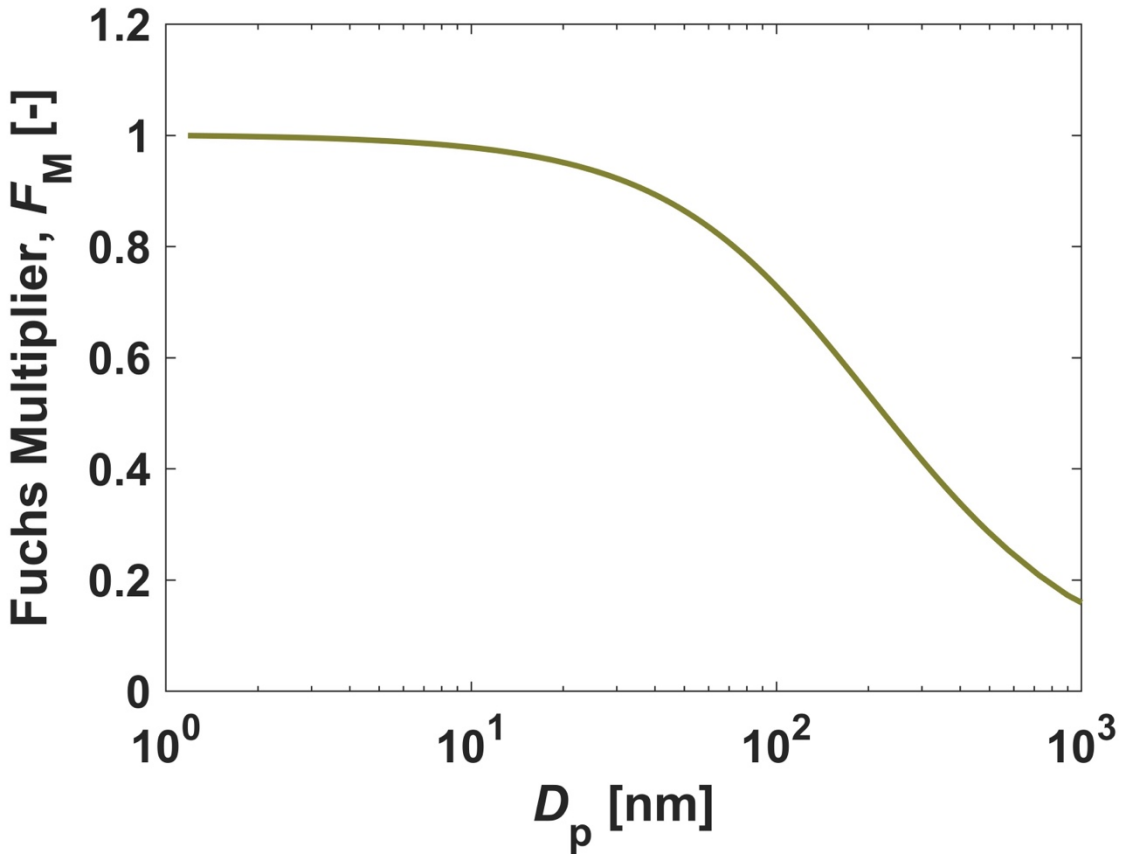

Figure S5. Variation of the Fuchs multiplier with particle diameter.

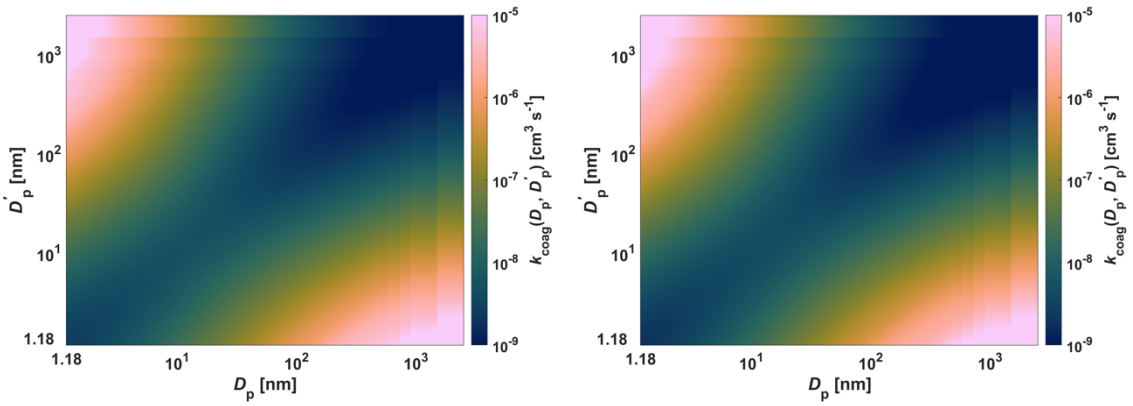

Figure S6. Coagulation coefficients for (left) boiling water and (right) cooking events considering the Hamaker constants listed in Table S3.

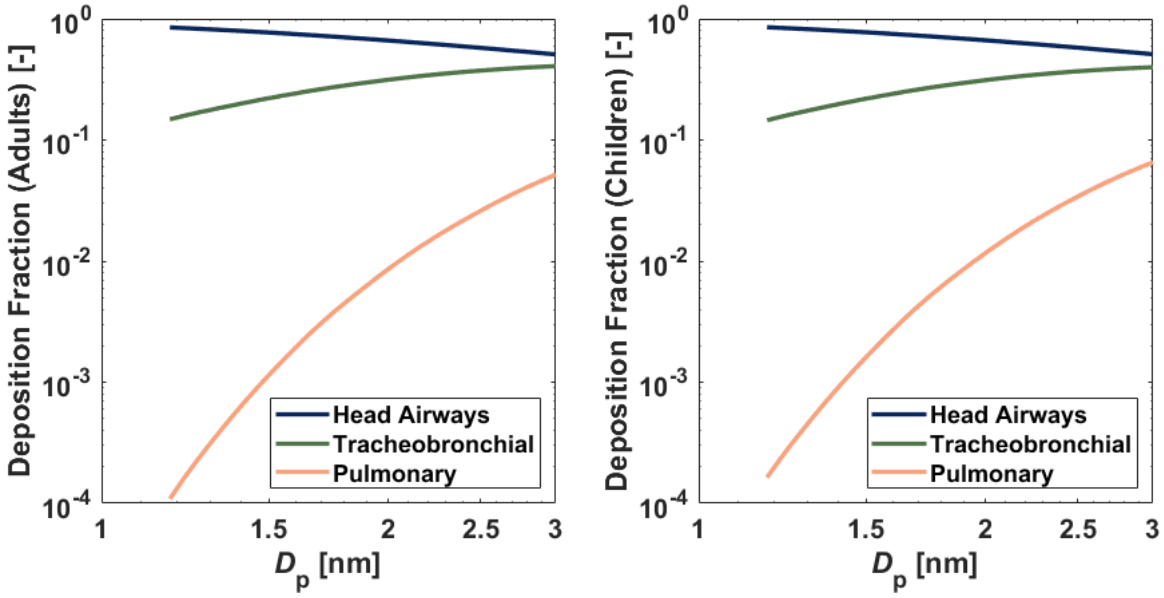

Figure S7. Size-resolved NCA deposition fractions for different human respiratory tract regions for (left) adults and (right) children. Deposition fractions were obtained from the Multiple-Path Particle Dosimetry (MPPD) model using the breathing parameters listed in Table S9.

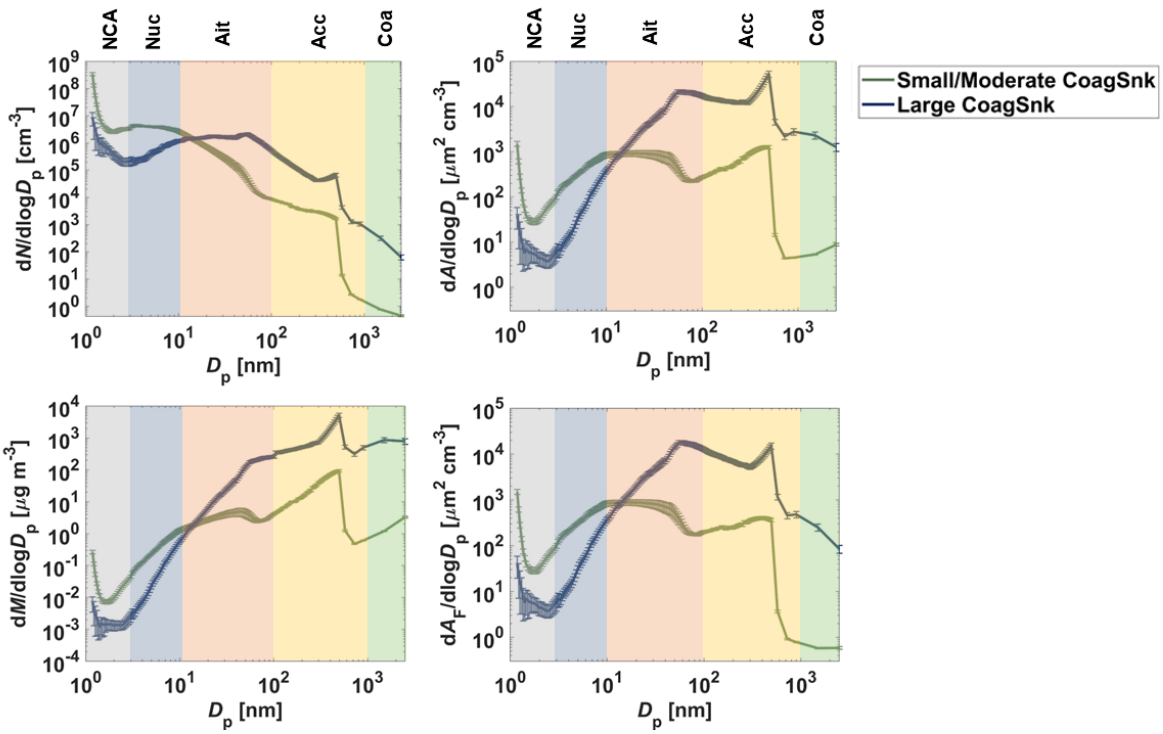

Figure S8. Mean (top left) particle number size distributions, (top right) particle surface area size distributions, (bottom left) particle mass size distributions, and (bottom right) particle Fuchs surface area size distributions during propane gas cooking for small/moderate indoor CoagSnk cases and large indoor CoagSnk cases. The error bars represent the standard errors (NCA: nanocluster aerosol; Nuc: nucleation mode aerosol; Ait: Aitken mode aerosol; Acc: accumulation mode aerosol; Coa: coarse mode aerosol).

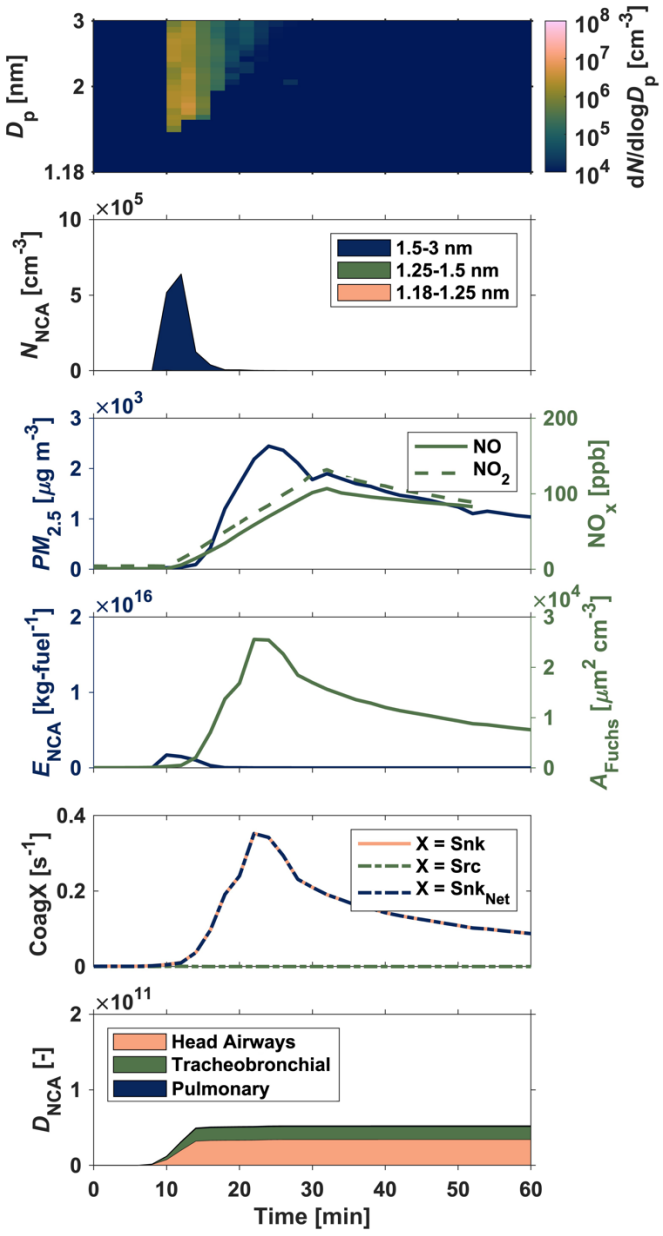

Figure S9. Time-resolved evaluation of indoor atmospheric NCA formation and transformation via high-resolution online nanoparticle measurements during propane gas cooking: (first row) propane gas cooking-emitted NCA number size distributions (dN/dlogD_p); (second row) Size-integrated (1.18–3 nm) propane gas cooking-emitted NCA number concentrations (N_{NCA}); (third row) Conventional indoor air pollution markers: $PM_{2.5}$ mass concentrations and NO + NO_2 mixing ratios; (fourth row) Carbon mass-based (1.18–3 nm) propane gas cooking-emitted NCA emission factors (E_{NCA}) and the aerosol Fuchs surface area (A_{Fuchs}); (fifth row) Coagulation sink, coagulation source, and the net difference between the coagulation sink and coagulation source; and (sixth row) Cumulative adult respiratory tract deposited doses (D_{NCA}) during the propane gas cooking measurements in the Purdue zEDGE test house (composite median of large indoor CoagSnk cases (cooking buttermilk pancakes)). The coagulation sink represents the median of the size-resolved coagulation sink values in the NCA size fraction. For X = Src, the coagulation source values are computed as the median of $CoagSrc_{dp}/N_{dp}$ over the NCA size fraction.

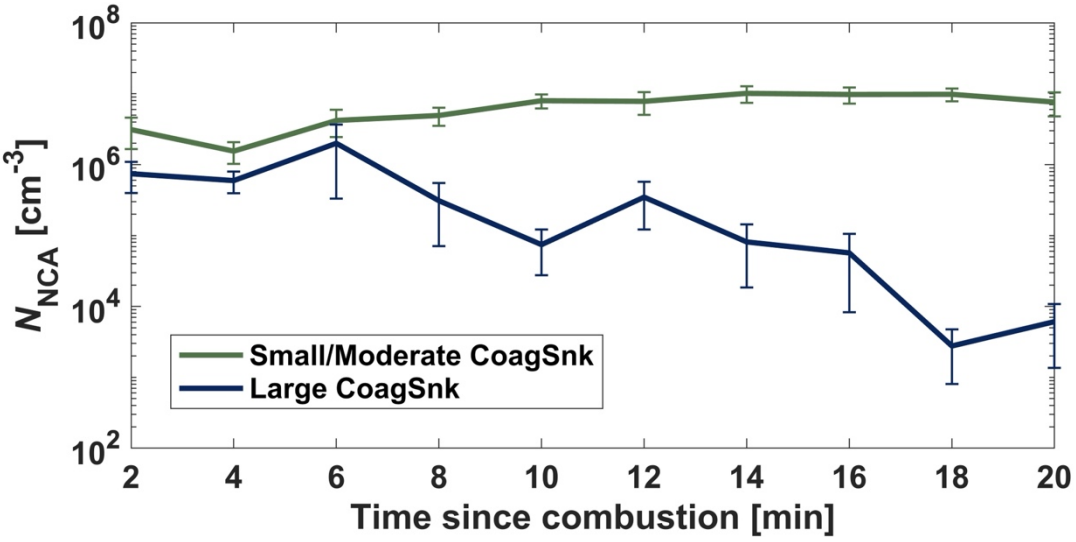

Figure S10. Comparison of size-integrated NCA number concentrations in the Purdue zEDGE test house during propane gas cooking for small/moderate CoagSnk and large CoagSnk cases. The solid continuous lines represent the mean of the size-integrated NCA number concentrations for each category of experiment, while the error bars represent the standard errors.

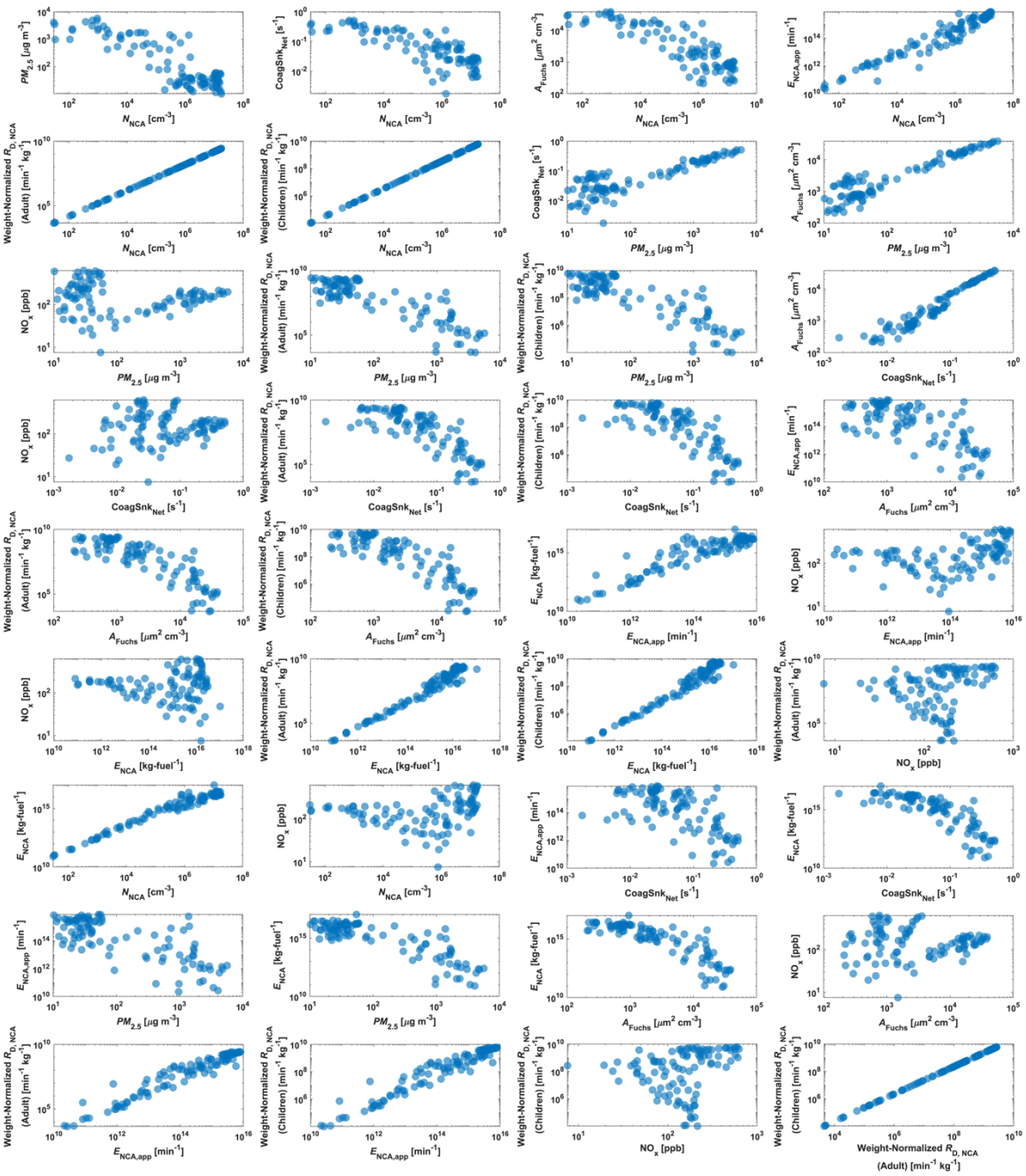

Figure S11. Relationships between different variables during active propane gas combustion periods across all experiments.

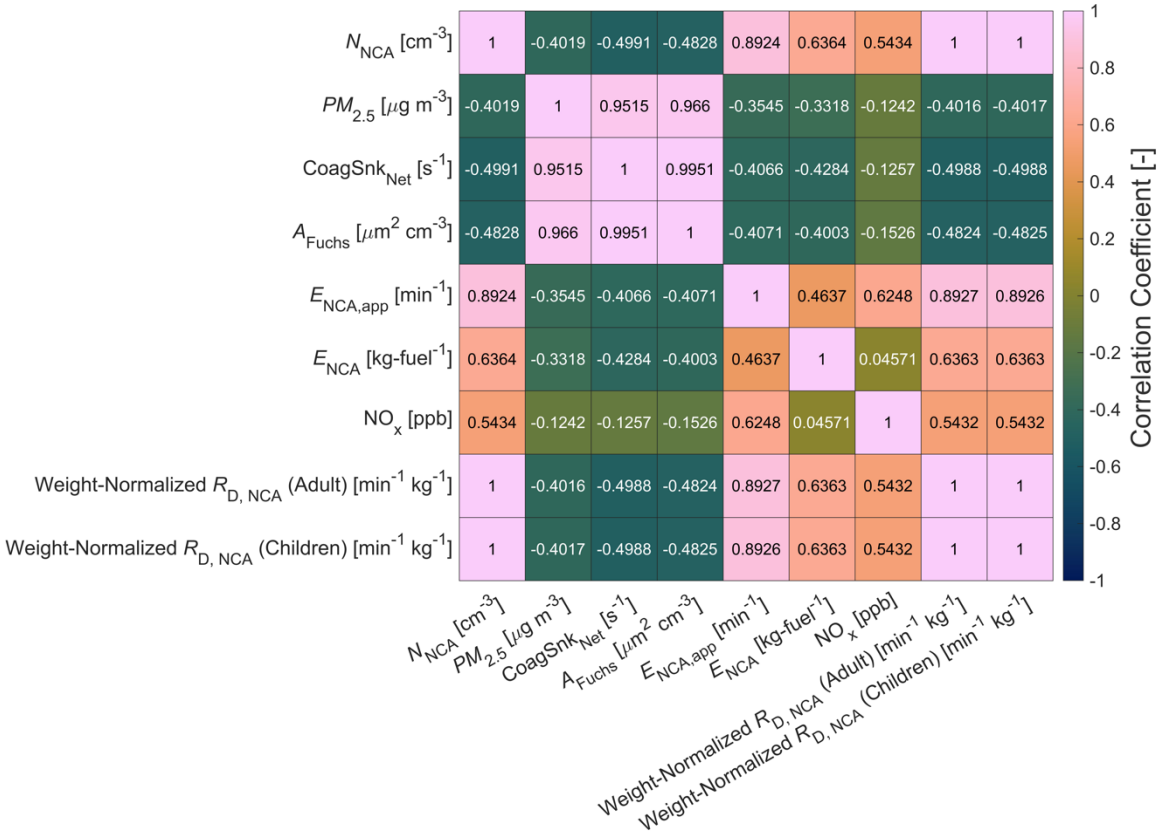

Figure S12. Correlation coefficient table for relationships between different variables during active propane gas combustion periods across all experiments.

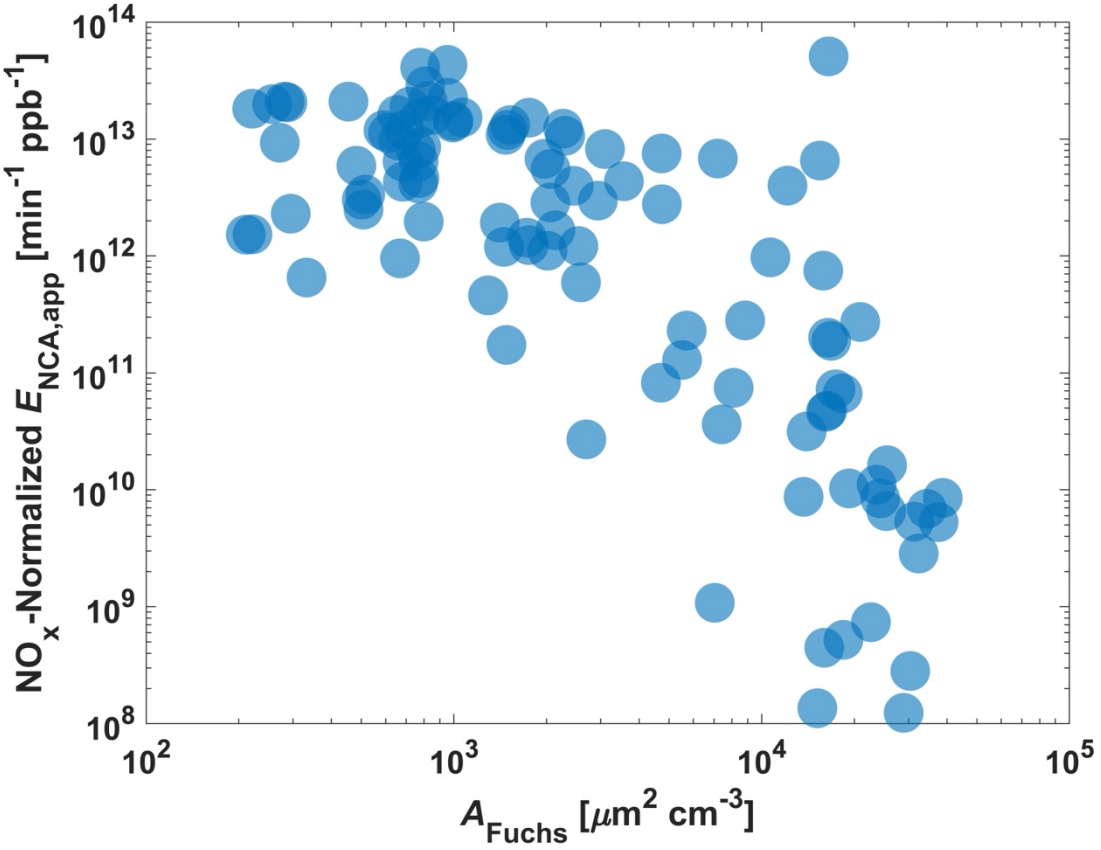

Figure S13. Relationship between the NO_x-normalized size-integrated propane gas cooking NCA apparent emission rate and the aerosol Fuchs surface area.

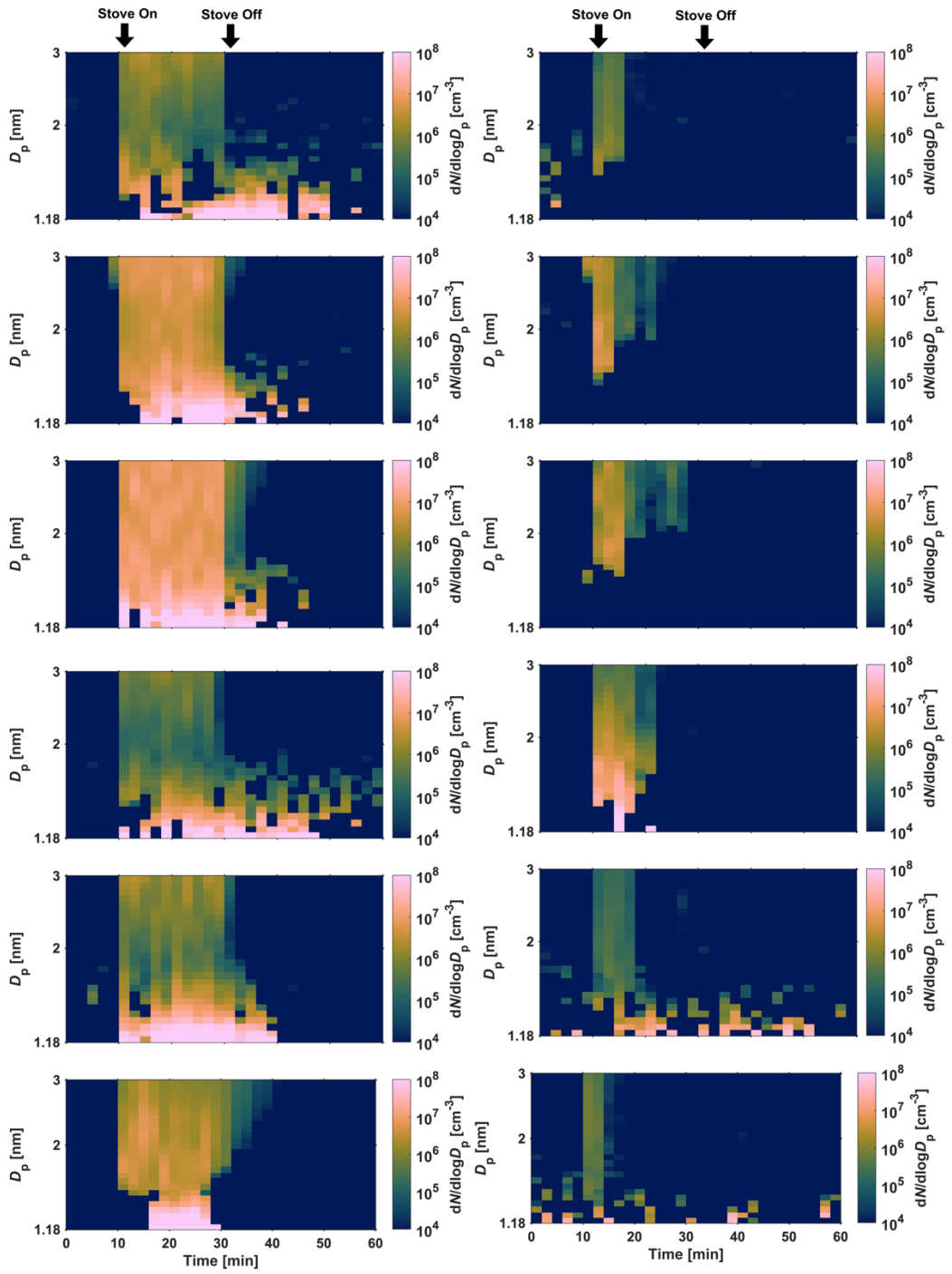

Figure S14. Time-resolved evaluation of propane gas cooking-emitted NCA number size distributions (dN/dlogD_p) from all 12 experiments conducted in this study. The left column displays results for low/moderate CoagSnk experiments, while the right column presents results for large CoagSnk experiments. The top three plots in the right column are related to cooking buttermilk pancakes, and the bottom three are related to cooking grilled cheese.

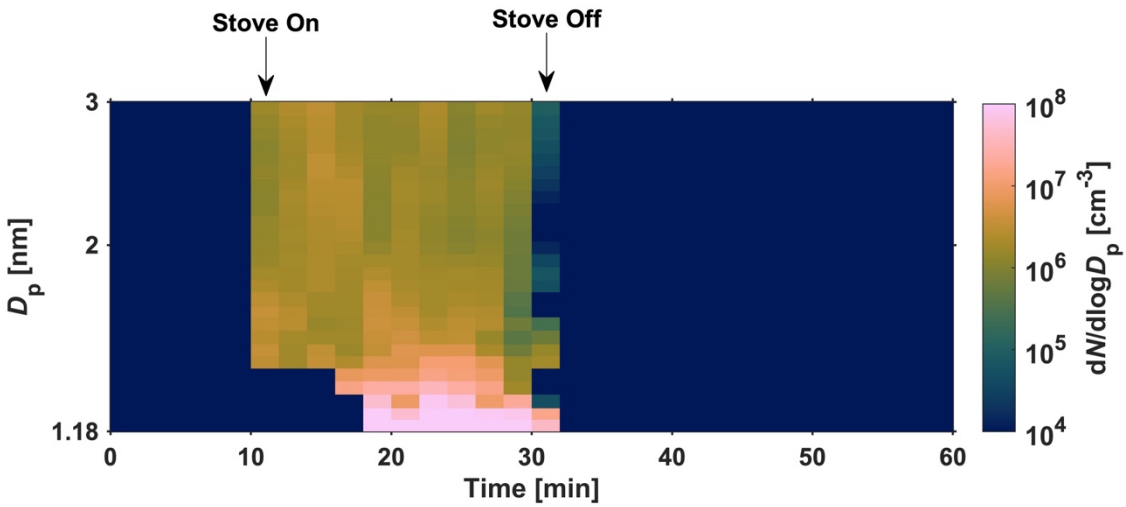

Figure S15. Median time-resolved evolution of propane gas cooking-emitted NCA number size distributions ($dN/d\log D_p$) across all low/moderate CoagSnk measurements obtained by employing the 99th percentile threshold in the charger ion correction.

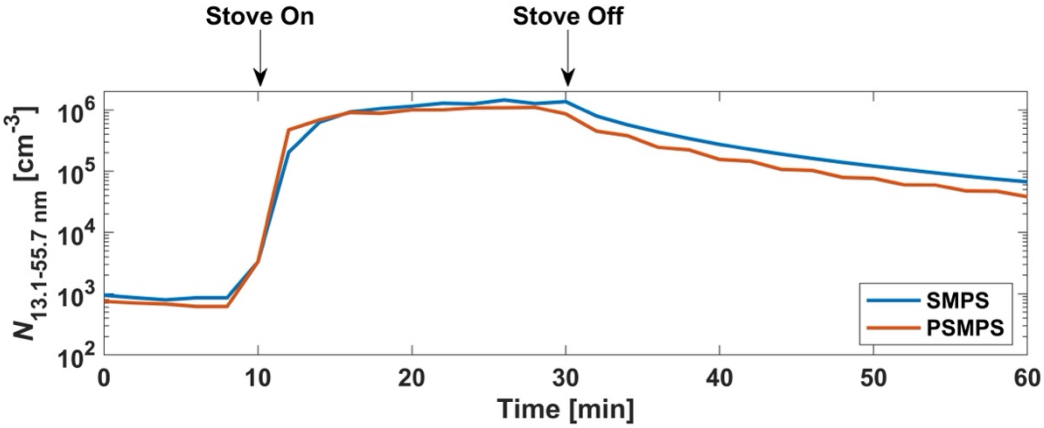

Figure S16. Comparison of size-integrated particle number concentrations in the overlapping size ranges of the SMPS and PSMPS (13.1 to 55.7 nm) in the Purdue zEDGE test house during a representative propane gas cooking experiment.

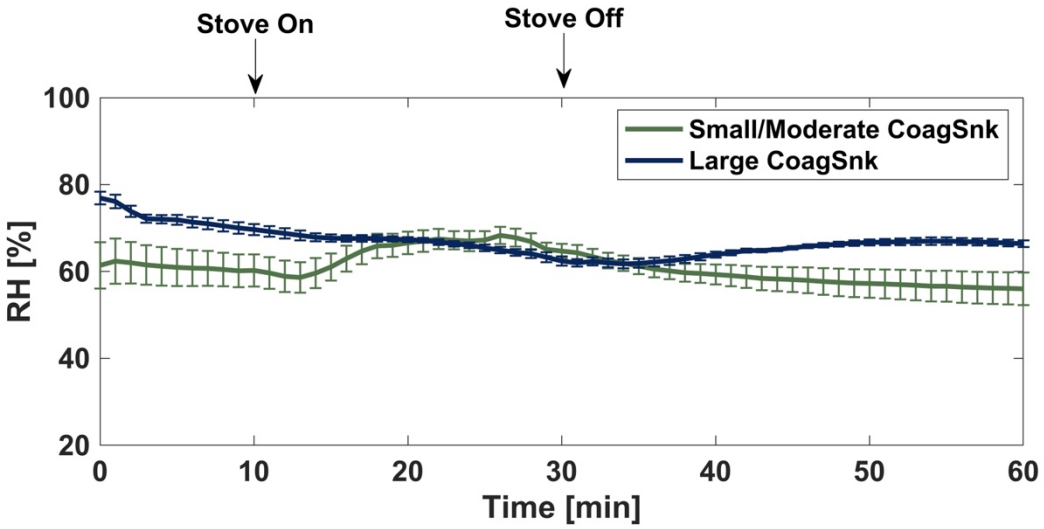

Figure S17. Time-resolved variation in the indoor RH in the Purdue zEDGE test house during propane gas cooking measurements for small/moderate CoagSnk and large CoagSnk cases. The solid lines represent the mean value across all experiments, and the error bars represent the standard errors.

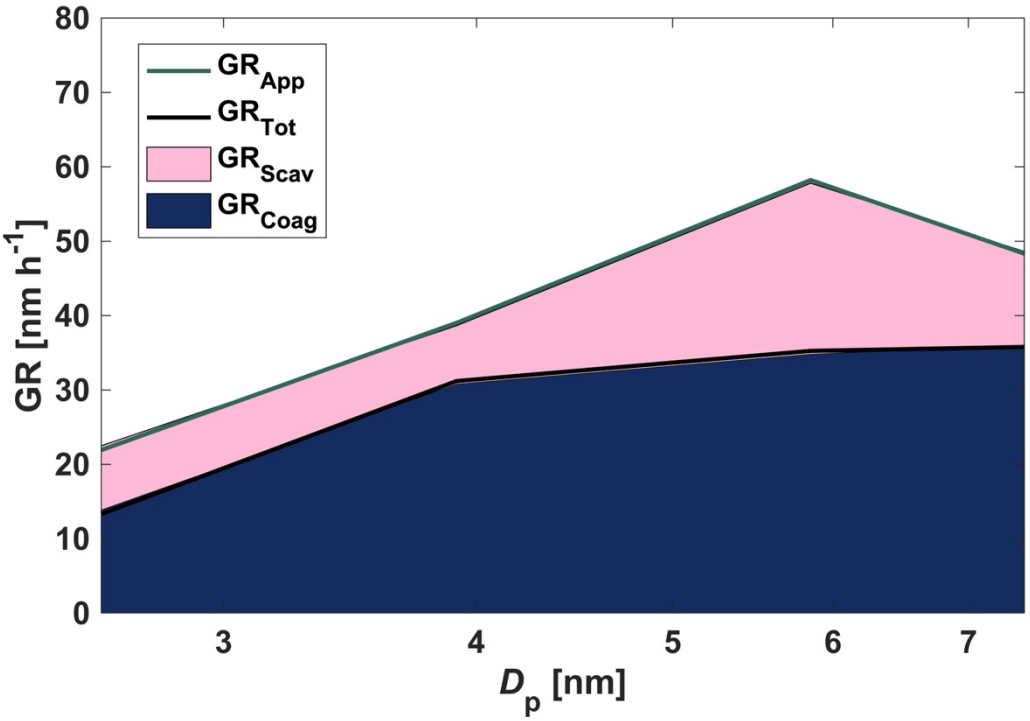

Figure S18. Size-resolved intramodal coagulation growth rate (GR_{Coag}), intermodal coagulation growth rate (GR_{Scav}), apparent growth rate (GR_{App}), and total growth rate (GR_{Tot}) for a representative boiling water experiment with the best fit Hamaker constant (A = 2.6 x 10^{-19} J).

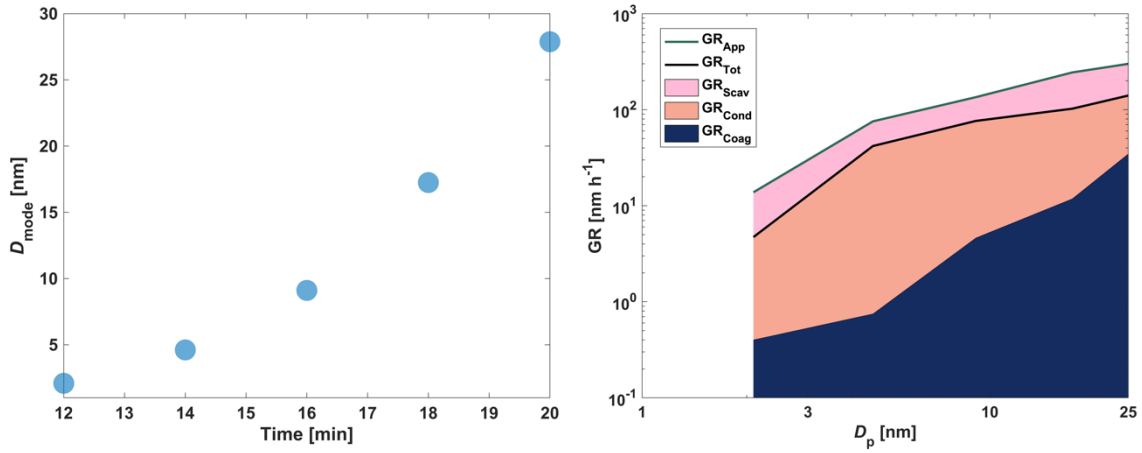

Figure S19. (left) Temporal evolution of D_{mode} in the mode-fitting method for a representative butter-based cooking measurement and (right) size-resolved GR_{Coag}, GR_{Cond}, GR_{Scav}, GR_{Tot}, and GR_{App} calculated for the same experiment.

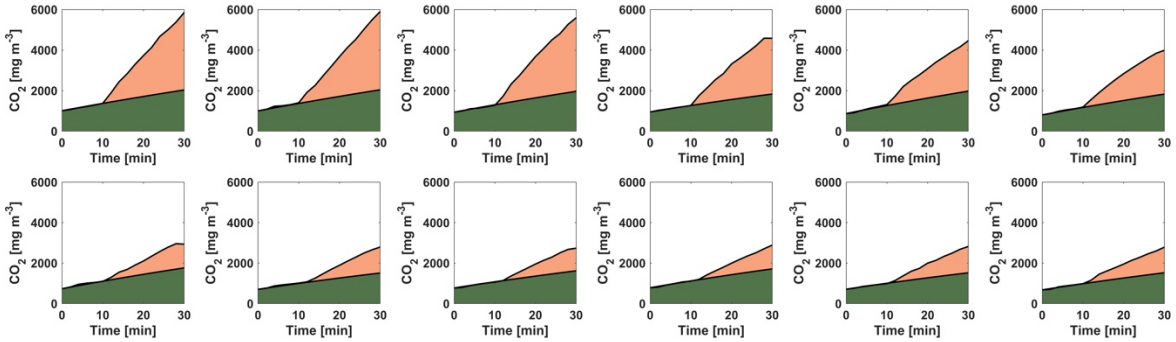

Figure S20. Time-resolved CO_2 concentrations in the Purdue zEDGE test house during all propane gas cooking experiments (top row: small/moderate CoagSnk cases; bottom row: large CoagSnk cases). The gas stove was ignited at the 10-minute mark and turned off at the 30-minute mark. Before that, the test house was occupied by two occupants. The green-colored area represents the CO_2 flux from outdoor air ventilation and occupant emissions (via exhaled breath). The peach-colored area represents the background-corrected CO_2 concentrations.

Table S1. Summary of the propane gas cooking events evaluated in the Purdue zEDGE test house.

ID	Cooking Activity with Gas Combustion	Outdoor Air Ventilation Rate [h^{-1}]	Mean T [°C]	Mean RH [%]	Peak N_{NCA} [cm^{-3}]	Mean N_{NCA} (std error) [cm^{-3}]
1A	Boiling Water	0.36	22.11	54.08	4.7×10^6	$1.9\ (0.4) \times 10^6$
1B	Boiling Water	0.33	22.57	52.88	1.8×10^7	$1.0\ (0.2) \times 10^7$
1C	Boiling Water	0.38	21.30	64.82	1.5×10^7	$1.1\ (0.1) \times 10^7$
2A	Boiling Water	0.51	18.96	73.26	4.6×10^6	$2.2\ (0.5) \times 10^6$
2B	Boiling Water	0.44	20.19	68.68	1.5×10^7	$8.7\ (1.4) \times 10^6$
2C	Boiling Water	0.45	19.35	61.14	1.7×10^7	$8.7\ (1.9) \times 10^6$
3A	Cooking Buttermilk Pancakes	0.49	19.20	64.26	2.0×10^5	$3.6\ (2.3) \times 10^4$
3B	Cooking Buttermilk Pancakes	0.52	17.97	66.10	7.7×10^5	$1.0\ (0.8) \times 10^5$
3C	Cooking Buttermilk Pancakes	0.47	19.26	67.94	8.2×10^5	$1.9\ (1.1) \times 10^5$
4A	Cooking Grilled Cheese	0.48	18.73	66.48	1.0×10^7	$1.6\ (1.0) \times 10^6$
4B	Cooking Grilled Cheese	0.49	19.22	67.34	6.9×10^5	$2.8\ (0.7) \times 10^5$
4C	Cooking Grilled Cheese	0.49	18.96	67.55	3.0×10^5	$7.7\ (3.7) \times 10^4$

Table S2. Effective densities used for computation of $PM_{2.5}$ mass concentrations.

Event Type	Effective Density [g cm^{-3}]	Reference
Boiling Water	0.9	Slowik et al. (34)
Cooking	0.9 ($1.18 < d_p \leq 100$ nm) 1.2 ($100 < d_p \leq 1000$ nm) 1.5 ($1000 < d_p \leq 2500$ nm)	Jiang et al. (35)

Table S3. Hamaker constants used for computation of the coagulation coefficient.

Event Type	Hamaker Constant [J]	Reference
Boiling Water	2.6×10^{-19}	-
Cooking	8.2×10^{-20}	Lai et al. (36)

Table S4. Sensitivity analysis of the size-integrated indoor atmospheric apparent NCA emission rate calculation for the cooking events.

$E_{NCA,app}$ [20 k_BT] [min^{-1}]	$E_{NCA,app}$ [200 k_BT] [min^{-1}]	Error [%]
2.31 x 10^{13}	2.76 x 10^{13}	19.49
1.80 x 10^{14}	2.07 x 10^{14}	14.99
5.57 x 10^{12}	6.53 x 10^{12}	17.22
3.34 x 10^{12}	3.84 x 10^{12}	14.95
3.21 x 10^{13}	3.70 x 10^{13}	15.26
1.35 x 10^{14}	1.55 x 10^{14}	14.81
2.17 x 10^{10}	2.65 x 10^{10}	22.13
8.26 x 10^{10}	9.77 x 10^{10}	18.27
9.65 x 10^{12}	1.10 x 10^{13}	13.98
7.19 x 10^{12}	7.94 x 10^{12}	10.43
9.47 x 10^{11}	9.51 x 10^{11}	0.43
1.93 x 10^{11}	2.05 x 10^{11}	6.20
8.86 x 10^{11}	1.11 x 10^{12}	25.73
1.07 x 10^{12}	1.28 x 10^{12}	19.68
4.41 x 10^{10}	5.18 x 10^{10}	17.46
5.07 x 10^{11}	5.92 x 10^{11}	16.76
1.38 x 10^{12}	1.60 x 10^{12}	15.89
2.66 x 10^{10}	3.04 x 10^{10}	14.27

Table S5. Sensitivity analysis of the net indoor coagulation sink calculation for the cooking events.

$CoagSnk_{Net}$ [20 k_BT] [s^{-1}]	$CoagSnk_{Net}$ [200 k_BT] [s^{-1}]	Error [%]
0.011	0.013	27.05
0.034	0.041	20.08
0.068	0.082	20.66
0.104	0.124	18.78
0.125	0.150	19.68
0.151	0.180	19.38
0.210	0.249	18.46
0.221	0.261	18.06
0.217	0.253	16.24
0.004	0.006	26.62
0.022	0.028	23.22
0.096	0.114	18.00
0.191	0.229	19.75
0.333	0.397	19.27
0.402	0.472	17.50
0.421	0.490	16.47
0.437	0.506	15.69
0.354	0.405	14.25

Table S6. Comparison of NCA number concentrations from propane gas cooking as measured in this study with NCA number concentrations reported for different environments.

Study	N_{NCA} [cm^{-3}]
Indoor NCA: propane gas cooking – small/moderate indoor CoagSnk cases (this study)	7×10^6 (mean)
Indoor NCA: propane gas cooking – large indoor CoagSnk cases (this study)	4×10^5 (mean)
Indoor NCA: skin oil ozonolysis in the presence of four human volunteers (37)	~10^2
Indoor NCA: modern preschools (38)	~2×10^6
Indoor NCA: monoterpene ozonolysis during floor mopping (39)	~10^5
Indoor NCA: 3D printing (40)	~10^2-10^5
Chamber NCA: cookstove emissions in a combustion chamber (31)	10^6-10^7
Outdoor NCA: traffic-influenced areas (41)	10^4-10^5
Outdoor NCA: rural environments (42)	10^2-10^4
Outdoor NCA: suburban and urban environments (42)	~10^2-10^5

Table S7. Comparison of atmospheric NCA emission factors from propane gas cooking as measured in this study with NCA emission factors reported for other combustion sources.

Study	Source	Particle Size Range	Instrument	E_{NCA} x 10^{15} (kg-fuel^{-1})
This Study	Propane gas cooking (small/moderate CoagSnk)	1.18 – 3 nm	PSMPS	0.70 – 30
	Propane gas cooking (large CoagSnk)			0.0001 – 20
Oikarinen et al., 2022 (43)	Gasoline vehicles	1.3 – 2.5 nm	A11-nCNC	0.13
	Diesel vehicles			0.35
Gren et al., 2021* (44)	Diesel engine	1.2 – 3 nm	A11-nCNC	0.20 – 2
Jathar et al., 2020 (31)	Three-stone fire	1.1 – 11 nm	A11-nCNC	4.80
	Rocket elbow			5.40
	Gasifier			8.50
	Charcoal			33.00
	LPG			18.90
Järvinen et al., 2019 (45)	Diesel buses	1.3 – 3 nm	A11-nCNC	0.20 – 8
Hietikko et al., 2018 (46)	Street canyon	1 – 3 nm	A11-nCNC	0.90
Rönkkö et al., 2017 (41)	Traffic	1.3 – 3 nm	A11-nCNC	2.40
	Street canyon			2.90
	Diesel engine			0.001 – 4.30

*Assuming fuel consumption: 0.2 kg kWh^{-1}

Table S8. PSMPS NCA size bins.

i	Midpoint Diameter [d_p; nm]	Lower Limit [d_l; nm]	Upper Limit [d_u; nm]
1	1.18	1.15	1.20
2	1.22	1.20	1.24
3	1.26	1.24	1.29
4	1.31	1.29	1.33
5	1.36	1.33	1.38
6	1.41	1.38	1.43
7	1.46	1.43	1.49
8	1.51	1.49	1.54
9	1.57	1.54	1.60
10	1.63	1.60	1.65
11	1.69	1.65	1.72
12	1.75	1.72	1.78
13	1.81	1.78	1.84
14	1.88	1.84	1.91
15	1.95	1.91	1.98
16	2.02	1.98	2.05
17	2.09	2.05	2.13
18	2.17	2.13	2.21
19	2.25	2.21	2.29
20	2.33	2.29	2.37
21	2.41	2.37	2.46
22	2.50	2.46	2.55
23	2.60	2.55	2.64
24	2.69	2.64	2.74
25	2.79	2.74	2.84
26	2.89	2.84	2.94
27	3.00	2.94	3.05

Table S9. Summary of breathing parameters and body weights used in the NCA respiratory tract deposited dose rate analysis.

Group	Inhalation Rate [cm^3 min^{-1}]	Breathing Frequency [breaths min^{-1}]	Tidal Volume [cm^3]	Body Weight [kg]
Children (47, 48)	11000	24	458.33	31.8
Adults (47–49)	12000	16.1	745.34	78.4

Supporting Information References

1. X. Ding, *et al.*, Evaluation of Workplace Exposures to Volatile Chemicals During COVID-19 Building Disinfection Activities with Proton Transfer Reaction Mass Spectrometry. *Ann Work Expo Health*, wxac096 (2023).
2. J. Jiang, *et al.*, Real-Time Measurements of Botanical Disinfectant Emissions, Transformations, and Multiphase Inhalation Exposures in Buildings. *Environ Sci Technol Lett* **8**, 558–566 (2021).
3. J. Jiang, *et al.*, Ethanol-based disinfectant sprays drive rapid changes in the chemical composition of indoor air in residential buildings. *Journal of Hazardous Materials Letters* **2**, 100042 (2021).
4. G. Steiner, H. Flentje, M. Väkevä, L. Keck, J. Vanhanen, Monitoring ambient aerosol size distributions from 1 - 55 nm with the GRIMM-AIRMODUS PSMPS in *EGU General Assembly Conference Abstracts*, (2021), pp. EGU21-12472.
5. S. S. Patra, T. Wu, D. N. Wagner, J. Jiang, B. E. Boor, Real-time measurements of fluorescent aerosol particles in a living laboratory office under variable human occupancy and ventilation conditions. *Build Environ* **205**, 108249 (2021).
6. P. G. Gormley, M. Kennedy, Diffusion from a Stream Flowing through a Cylindrical Tube. *Proceedings of the Royal Irish Academy. Section A: Mathematical and Physical Sciences* **52**, 163–169 (1948).
7. M. He, S. Dhaniyala, Experimental characterization of flowrate-dependent bipolar diffusion charging efficiencies of sub-50nm particles. *J Aerosol Sci* **76**, 175–187 (2014).
8. J. Kangasluoma, *et al.*, Remarks on Ion Generation for CPC Detection Efficiency Studies in Sub-3-nm Size Range. *Aerosol Science and Technology* **47**, 556–563 (2013).
9. D. Stolzenburg, G. Steiner, P. M. Winkler, A DMA-train for precision measurement of sub-10nm aerosol dynamics. *Atmos Meas Tech* **10**, 1639–1651 (2017).
10. L. A. Sgro, A. De Filippo, Size Distribution Measurements of Nanoparticles of Organic Carbon in Hydrocarbon-Air Flames in *30th Meeting on Combustion Italian Section of the Combustion Institute (2007b) Ischia, Italy*, (2007).
11. V. Premnath, D. Oberreit, C. J. H. Jr., Collision-Based Ionization: Bridging the Gap between Chemical Ionization and Aerosol Particle Diffusion Charging. *Aerosol Science and Technology* **45**, 712–726 (2011).
12. M. Attoui, J. Fernández-García, J. Cuevas, G. Vidal-de-Miguel, J. Fernandez de la Mora, Charge evaporation from nanometer polystyrene aerosols. *J Aerosol Sci* **55**, 149–156 (2013).
13. L. A. Sgro, A. D'Anna, P. Minutolo, Charge Distribution of Incipient Flame-Generated Particles. *Aerosol Science and Technology* **44**, 651–662 (2010).
14. E. Vo, M. Horvatin, Z. Zhuang, Performance Comparison of Field Portable Instruments to the Scanning Mobility Particle Sizer Using Monodispersed and Polydispersed Sodium Chloride Aerosols. *Ann Work Expo Health* **62**, 711–720 (2018).
15. A. S. Fonseca, *et al.*, Intercomparison of a portable and two stationary mobility particle sizers for nanoscale aerosol measurements. *Aerosol Science and Technology* **50**, 653–668 (2016).
16. T.-C. Hsiao, *et al.*, Experimental Comparison of Two Portable and Real-Time Size Distribution Analyzers for Nano/Submicron Aerosol Measurements. *Aerosol Air Qual Res* **16**, 919–929 (2016).
17. R. Cai, *et al.*, Aerosol surface area concentration: a governing factor in new particle formation in Beijing. *Atmos Chem Phys* **17**, 12327–12340 (2017).
18. L. Dada, *et al.*, Formation and growth of sub-3-nm aerosol particles in experimental chambers. *Nat Protoc* **15**, 1013–1040 (2020).
19. M. Kulmala, *et al.*, Measurement of the nucleation of atmospheric aerosol particles. *Nat Protoc* **7**, 1651–1667 (2012).
20. M. Dal Maso, *et al.*, Condensation and coagulation sinks and formation of nucleation mode particles in coastal and boreal forest boundary layers. *Journal of Geophysical Research: Atmospheres* **107**, PAR 2-1-PAR 2-10 (2002).
21. R. Cai, J. Jiang, A new balance formula to estimate new particle formation rate: reevaluating the effect of coagulation scavenging. *Atmos Chem Phys* **17**, 12659–12675 (2017).

22. A. C. K. Lai, W. W. Nazaroff, MODELING INDOOR PARTICLE DEPOSITION FROM TURBULENT FLOW ONTO SMOOTH SURFACES. *J Aerosol Sci* **31**, 463–476 (2000).
23. D. Rim, J.-I. Choi, L. A. Wallace, Size-Resolved Source Emission Rates of Indoor Ultrafine Particles Considering Coagulation. *Environ Sci Technol* **50**, 10031–10038 (2016).
24. R. Zhang, *et al.*, Variability in morphology, hygroscopicity, and optical properties of soot aerosols during atmospheric processing. *Proceedings of the National Academy of Sciences* **105**, 10291–10296 (2008).
25. D. Stolzenburg, *et al.*, Atmospheric nanoparticle growth. *Rev Mod Phys* **95**, 45002 (2023).
26. J. Leppä, T. Anttila, V.-M. Kerminen, M. Kulmala, K. E. J. Lehtinen, Atmospheric new particle formation: real and apparent growth of neutral and charged particles. *Atmos Chem Phys* **11**, 4939–4955 (2011).
27. R. Cai, *et al.*, Impacts of coagulation on the appearance time method for new particle growth rate evaluation and their corrections. *Atmos Chem Phys* **21**, 2287–2304 (2021).
28. G. De Falco, M. Commodo, P. Minutolo, A. D'Anna, Flame-Formed Carbon Nanoparticles: Morphology, Interaction Forces, and Hamaker Constant from AFM. *Aerosol Science and Technology* **49**, 281–289 (2015).
29. C. G. Masoud, *et al.*, Molecular composition and gas-particle partitioning of indoor cooking aerosol: Insights from a FIGAERO-CIMS and kinetic aerosol modeling. *Aerosol Science and Technology* **56**, 1156–1173 (2022).
30. D. Rim, M. Green, L. Wallace, A. Persily, J.-I. Choi, Evolution of Ultrafine Particle Size Distributions Following Indoor Episodic Releases: Relative Importance of Coagulation, Deposition and Ventilation. *Aerosol Science and Technology* **46**, 494–503 (2012).
31. S. H. Jathar, *et al.*, Emissions and radiative impacts of sub-10 nm particles from biofuel and fossil fuel cookstoves. *Aerosol Science and Technology* **54**, 1231–1243 (2020).
32. M. Sakamoto, *et al.*, CO2 emission rates from sedentary subjects under controlled laboratory conditions. *Build Environ* **211**, 108735 (2022).
33. T. Wu, *et al.*, Infant and Adult Inhalation Exposure to Resuspended Biological Particulate Matter. *Environ Sci Technol* **52**, 237–247 (2018).
34. J. G. Slowik, *et al.*, An Inter-Comparison of Instruments Measuring Black Carbon Content of Soot Particles. *Aerosol Science and Technology* **41**, 295–314 (2007).
35. J. Jiang, N. Jung, B. E. Boor, Using Building Energy and Smart Thermostat Data to Evaluate Indoor Ultrafine Particle Source and Loss Processes in a Net-Zero Energy House. *ACS ES&T Engineering* **1**, 780–793 (2021).
36. A. C. K. Lai, J. Chen, Numerical study of cooking particle coagulation by using an Eulerian model. *Build Environ* **89**, 38–47 (2015).
37. S. Yang, *et al.*, Ozone Initiates Human-Derived Emission of Nanocluster Aerosols. *Environ Sci Technol* **55**, 14536–14545 (2021).
38. M. Amouei Torkmahalleh, *et al.*, Formation of cluster mode particles (1–3 nm) in preschools. *Science of The Total Environment* **818**, 151756 (2022).
39. C. M. F. Rosales, *et al.*, Chemistry and human exposure implications of secondary organic aerosol production from indoor terpene ozonolysis. *Sci Adv* **8**, eabj9156 (2023).
40. M. Poikkimäki, *et al.*, Nanocluster Aerosol Emissions of a 3D Printer. *Environ Sci Technol* **53**, 13618–13628 (2019).
41. T. Rönkkö, *et al.*, Traffic is a major source of atmospheric nanocluster aerosol. *Proceedings of the National Academy of Sciences* **114**, 7549–7554 (2017).
42. J. Kontkanen, *et al.*, Measurements of sub-3nm particles using a particle size magnifier in different environments: from clean mountain top to polluted megacities. *Atmos Chem Phys* **17**, 2163–2187 (2017).
43. H. Oikarinen, *et al.*, Particle number, mass, and black carbon emissions from fuel-operated auxiliary heaters in real vehicle use. *Atmos Environ X* **16**, 100189 (2022).
44. L. Gren, *et al.*, Effects of renewable fuel and exhaust aftertreatment on primary and secondary emissions from a modern heavy-duty diesel engine. *J Aerosol Sci* **156**, 105781 (2021).
45. A. Järvinen, *et al.*, Particle emissions of Euro VI, EEV and retrofitted EEV city buses in real traffic. *Environmental Pollution* **250**, 708–716 (2019).
46. R. Hietikko, *et al.*, Diurnal variation of nanocluster aerosol concentrations and emission factors in a street canyon. *Atmos Environ* **189**, 98–106 (2018).

47. U.S. EPA, “Exposure Factors Handbook 2011 Edition (Final Report)” (2011).
48. F. J. Miller, B. Asgharian, J. D. Schroeter, O. Price, Improvements and additions to the Multiple Path Particle Dosimetry model. *J Aerosol Sci* **99**, 14–26 (2016).
49. B.-S. Lin, R.-J. Jhang, B.-S. Lin, Wearable Cardiopulmonary Function Evaluation System for Six-Minute Walking Test. *Sensors* **19** (2019).